FOREX Publication
Open Access | Rapid and quality publishing

International Journal of
Electrical and Electronics Research (IJEER)
Research Article | Volume 14, Issue 1| Pages 38-55|e-ISSN: 2347-470X

Adaptive Fuzzy Network Denoising for Enhanced Thin Ice Visualization in Cross-Polarized Sentinel-1 SAR

Halit NAZLI[1], Osman YILDIRIM[2*]

[1,2]Electrical Electronic Engineering, Istanbul Aydin University, Istanbul, Turkey; Email: [1]khaledalnazli@stu.aydin.edu.tr; [2]osmanyildirim@aydin.edu.tr

***Correspondence:** *Halit NAZLI; khaledalnazli@stu.aydin.edu.tr*

ABSTRACT- Detecting thin (baby) ice in HV-polarized Sentinel-1 extra-wide (EW) sea-ice SAR images is challenging because thermal noise and the scalloping effect can mask weak backscatter signals. This paper proposes an adaptive denoising and thresholding approach using a self-designed fuzzy logic controller network (FLCN) to enhance baby-ice visualization. The approach automatically selects "no object" and "minimum object" regions and applies a data-driven correction factor to improve noise suppression without relying on external parameters. The FLCN generates input–output membership functions autonomously, reducing the need for manual tuning. We compare the results against the ESA/SNAP noise-vector correction workflow, a recent Q1 EW sea-ice denoising method [5], and a deep-learning denoiser (DnCNN). A quantitative and qualitative evaluation over multiple Sentinel-1 EW HV scenes using ROI-based open-water statistics (mean and standard deviation) and an SNR measure shows consistent noise suppression while preserving the ice–water boundaries compared to other recent methods.

Keywords: Thermal noise, Scalloping effect SAR, Fuzzy logic network, SAR, Speckles noise.

ARTICLE INFORMATION

Author(s): Halit NAZLI, and Osman YILDIRIM;
Received: 20/10/2025; **Accepted**: 29/01/2026; **Published**: 10/03/2026;
E- ISSN: 2347-470X;
Paper Id: IJEER2110A16
Citation: 10.37391/ijeer.140105
Webpage-link:
https://ijeer.forexjournal.co.in/archive/volume-14/ijeer-140105.html

Publisher's Note: FOREX Publication stays neutral with regard to jurisdictional claims in Published maps and institutional affiliations.

1. INTRODUCTION

Synthetic aperture radar (SAR), especially wide-beam dual-polarized C-band systems, plays a vital role in marine applications such as sea ice monitoring, oil spill detection, and ship tracking [1–5]. While co-polarized channels are more sensitive to environmental factors like wind and incidence angles, cross-polarized channels, though more stable in such condition, suffer from increased thermal noise and scalloping effects due to lower signal-to-noise ratios [6]. These artifacts degrade image quality and affect texture-based feature extraction crucial for sea ice analysis. Sentinel-1 partially mitigates scalloping through TOPSAR beam steering, but the issue remains. Although ESA provides scene-based noise vectors for correction, their accuracy and effectiveness can be inconsistent. Several approaches have been proposed to address these limitations, including morphological filtering for change detection [7], FIR filters for scalloping reduction [8], Kalman filtering [9], and deconvolution methods [10]. These methods demonstrate varying degrees of success but underscore the need for more adaptive and data-driven denoising strategies in SAR imagery. In [11], an efficient noise reduction method was proposed for Sentinel-1 GRD products, refining ESA-provided noise vectors with empirically derived correction coefficients.

This method addresses both range-dependent thermal noise and burst-time-dependent scalloping noise, enabling reconstruction of a complete noise field for subtraction and improving noise characteristics across different IPF versions. Park et al. [12] proposed adjusting ESA-provided noise vectors using a denoising scheme with scaling factors and power balancing, averaged across multiple scenes. Despite this, wide-beam SAR images often retain multiplicative residual noise, leading to textural artifacts. To address this, [13] introduced a method based on noise equivalent standard deviation (NESD). Building on these, [5] applied fifty scaling factors per sub-swath and scene, reducing inter-scan banding and improving prior techniques. An unsupervised despeckling framework for Sentinel-1 dual-polarization SAR was presented in [14], using a "noise image–noise image" strategy with a dual-branch network to preserve polarization while reducing speckle—suitable for medium- and low-resolution images. In our recent work [15], we addressed thermal noise by linearizing noise fields along the range and correcting azimuth slope to mitigate scalloping, using calm water regions for training. This improved signal-to-noise ratio, though residual noise remained.

This paper introduces a fuzzy logic network (FLN)-based denoising and thresholding approach for wide-beam SAR images. Fuzzy logic systems are well-suited for handling uncertainty and noise [15], [16], offering robustness in tasks like segmentation, edge detection, and thresholding [17]. Their adaptability allows for handling nonlinearity and ambiguous data, with human-like reasoning expressed through linguistic rules. In [18], a fuzzy inference system (FIS) enhanced edge detection through an open-loop controller, showing improved accuracy over traditional methods in Python and MATLAB

FOREX Publication
Open Access | Rapid and quality publishing
International Journal of Electrical and Electronics Research (IJEER)
Research Article | Volume 14, Issue 1| Pages 38-55|e-ISSN: 2347-470X

implementations. As per [19], SAR segmentation includes gray- and texture-level methods—both addressed in our work. A fuzzy filtering technique in [20] preserved fine details while denoising grayscale and color images, benefiting segmentation and object recognition. Lastly, [21] proposed a noise floor estimation model for Sentinel-1 GRD images, using power functions and weighted least squares to improve subswath-wise offset estimation. Recent developments in SAR image processing have introduced a variety of advanced techniques combining traditional methods with deep learning and fuzzy logic. HPHR-SAR-Net [22] integrates nonlocal total variation and nonconvex compound regularization into a deep unfolding network optimized *via* ADMM, enhancing resolution and computational efficiency while preserving phase information. Wang et al. [23] proposed CSHLC, a segmentation method that preserves small targets and corners under noise. A two-component deep learning network in [24] achieved real-time denoising using texture estimation and noise removal subnetworks, outperforming methods like PPB, SAR-POTDF, and SAR-BM3D. LG-DBNet [25] combined CNN-based local features with transformer-based global modeling, using hybrid attention and residual learning to minimize artifacts. A cGAN model in [26] integrated pix2pix and ResNet to enhance denoising and recognition accuracy with a parallel classifier. In [27], a machine learning pipeline fusing ICESat-2, Sentinel-1, and Sentinel-2 outperformed Landsat-8 in forest canopy height mapping. Fuzzy logic remains prominent: [28] used fuzzy-K-means for textured noise detection; [29] integrated fuzzy logic with the Perona-Malik algorithm; and [30] employed interval type-2 fuzzy sets for segmentation under uncertainty. A deep network in [31] combined fuzzy learning with graph reasoning for semantic segmentation. In [32-33], a fuzzy-weighted active contour model improved water/land classification using local entropy and variance. The Sugeno-type fuzzy controller (Takagi–Sugeno) provides an efficient alternative to Mamdani systems by using constants or functions in rule consequents, enabling real-time response. In zero-order SISO models, a single input maps to a constant output through fuzzy rules. For MISO systems, outputs are computed as weighted averages of multiple rules based on input combinations and aggregation functions, offering smooth control even in high-dimensional spaces.

Suppose we have n inputs: $x_1, x_2, \ldots, x_n$. R fuzzy rules.

Each Sugeno zero-order rule has the form:
Rule i: If x_1 is A_{i1} and x_2 is A_{i2} and ... and x_n is A_{in}, then $y_i = c_i$

Where: A_{ij}: fuzzy set for input x_j in rule i
c_i: constant output of rule i

The firing strength (or degree of activation) of rule i is calculated using a T-norm as expressed in *equations (1)* and *(2)*.

$$w_i = \mu\_A_{i1}(x_1) \times \mu\_A_{i2}(x_2) \times \ldots \times \mu\_A_{in}(x_n) \quad (1)$$

or

$$w_i = \prod \mu\_A_{ij}(x_j) \text{ for } j = 1 \text{ to } n \quad (2)$$

Where $\mu\_A_{ij}(x_j)$: is the membership value of input x_j in fuzzy set A_{ij}, w_i: Firing strength (activation level) of the i^{th} rule, and $\prod$: Product operator (multiply all terms)

Output Computation
The final output y is a weighted average of all the rule outputs can be expressed as the following equation:

$$y = (\Sigma w_i \times c_i) / (\Sigma w_i) \quad (3)$$

Where w_i: firing strength of rule i, c_i: constant output of rule i, y: Final crisp output of the fuzzy system, and Σ: Summation operator.

The inference mechanism evaluates all applicable rules simultaneously, determining the influence of each rule based on how well the input values match the conditions defined in the rules. Finally, the defuzzifier combines the outputs of all rules into a single crisp value by computing a weighted average, ensuring a smooth and precise control response suitable for real-time systems.

The remainder of this paper is organized as follows: *Section 2* introduces the correction factor used in the preprocessing stage to reduce the range depended noise fields. *Section 3* presents the proposed fuzzy logic network for enhancing the visualization of the thin ice regions in wide-beam SAR images. *Section 4* reports and discusses experimental results using real Sentinel-1 data. Finally, *section 5* concludes the paper and outlines potential directions for future work.

2. REDUCTION OF THE RANGE DEPENDED NOISE FIELDS

Thermal noise (TN) correction and noise subtraction are performed on calibrated data, specifically the sigma-nought values of SAR data. We used ESA SNAP software [34] to convert digital number (DN) pixel values to sigma-nought. Thermal noise can be considered an additive noise in the range direction, allowing for direct subtraction to denoise SAR scenes. Since the width of each sub-swath (SS) varies in the azimuth direction, an edge detection process is required.

The ESA-provided thermal noise (TN) matrix often leaves significant residual noise after subtraction. To improve suppression, a correction factor (CF) is applied to adjust the TN level for each sub swath. This involves identifying the minimum row in every 20-column segment by averaging row positions, producing a vector that represents the TN level across the scene (*Figure 3*). This method assumes the presence of at least one open-water row spanning the full range, though the step size (*e.g.*, 20 columns) can be adjusted as needed.

The CF was calculated for each SS, (for instance the first SS 0-2997 columns for the first area of the first scene), to ensure that the final TN would be either higher or equal to the averaged TN, we must ensure that the CF would be higher or equal to one. The used equation for calculating the CF is shown in *equation (4)*.

$$CF = \frac{\left(\frac{max(mean\ envelop)}{max(VM)} + \frac{\min(mean\ envelop)}{\min(VM)}\right)}{2} \quad (4)$$

For the first area (rows 1-3412) of the first scene the CF was found to be CF = [1.5241,1,1,1,1]. Then each CF would be

FOREX Publication
Open Access | Rapid and quality publishing
International Journal of Electrical and Electronics Research (IJEER)
Research Article | Volume 14, Issue 1| Pages 38-55|e-ISSN: 2347-470X

multiplied by the average TN (*e.g.*, 1.5241 would be multiplied by the averaged TN from 1-2997, and 1 multiplied by averaged TN (from 2998-4899, etc.). The final thermal noise (after CF multiplication) is shown in *figure 1*.

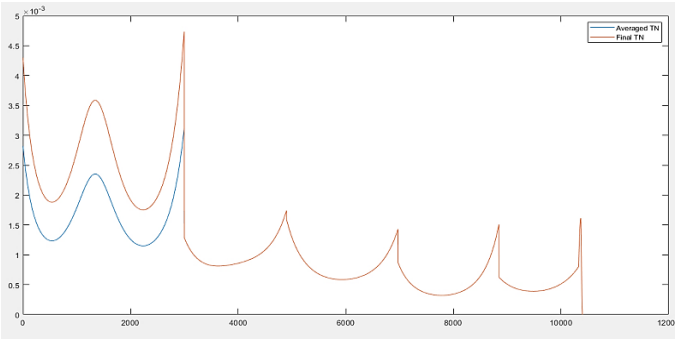

Figure 1. The final and the average TN

As the CF shows that for the first area only the first SS noise level was increased, the denoised scene by using the averaged TN and the CF TN are shown in *figure 2*.

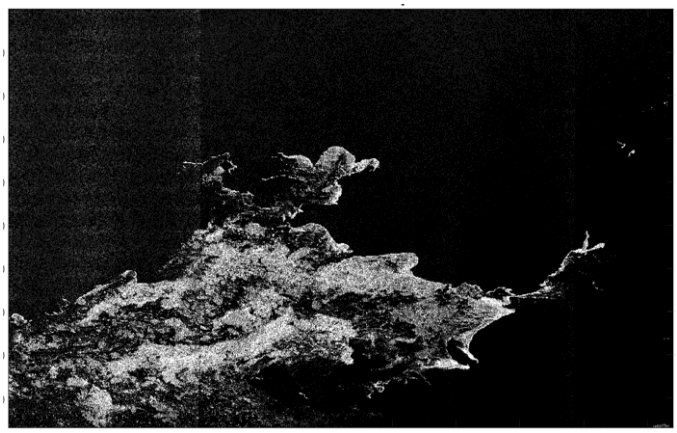

(a)

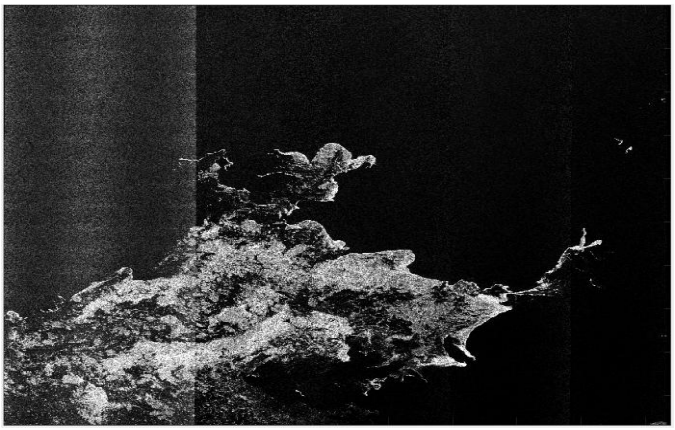

(b)

Figure 2. (a) and (b) are the denoised scene by CF TN and by the ESA provided TN respectively

As *figure 3* shows the minimum rows of the scene by using CF and without using CF.

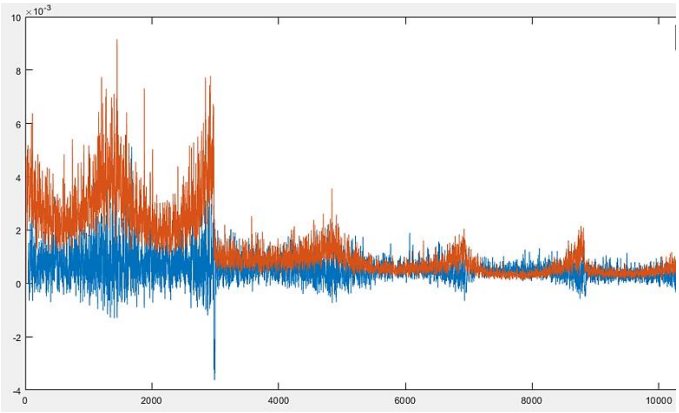

Figure 3. The VM before and after TN subtraction by using CF

As shown in *figure 3*, using the CF can decrease the remaining thermal noise (TN) by increasing the level of the average ESA TN, based on the maximum and minimum points of each interval, as described in *equation (5)*. However, the CF calculation can be based on either the maximum or the minimum points. Since the VM is constructed from the minimum rows, it is also reasonable to calculate the CF based on the maximum points of the averaged envelope and the VM, which results in CF = [2.0896, 1.2611, 0.9116, 1.0090, 0.5312].

$$CF(MAX) = \frac{max(mean\ envelop)}{ma\,x(VM)} \quad (5)$$

3. PROPOSED METHODOLOGY

The main aim of this study is to detect thin ice regions in sea ice SAR images since the detection of these regions is a challenging task, due to their low pixel intensity compared to thick ice and land regions. By knowing the thin ice regions any data losses could be avoidable in the denoising or filtering stage which will increase the quality of the final denoised scene. The proposed approach could be used to detect thin ice, open water and ice regions using fuzzy network (FN) as Figure 4 shows the configuration of the proposed method. Fuzzy logic systems are widely recognized for their ability to handle uncertainties and noise, making them ideal for tasks such as detecting regions with unclear boundaries, therefore it will be suitable for thin ice detection in SAR images.

After subtracting the noise matrices provided in the annotated files, the pre-denoised scene is obtained. The first step is to divide the image into regions of 20 columns and calculate the average value for each row in those regions. The result will be the Rows Average (RA) vector. Next, a sliding average filter of size 9x1 and step size 1 is applied to the RA to calculate the average kernel (AK), as shown in *figure 5*, with *equations (6)* and *(7)* describing the average filters. This step is repeated for each region in the scene. Then, the maximum and minimum locations of the AK are determined. These maximum and minimum locations will be used to extract features, which will then be used to build the FLC1.

FOREX Publication
Open Access | Rapid and quality publishing
International Journal of Electrical and Electronics Research (IJEER)
Research Article | Volume 14, Issue 1| Pages 38-55|e-ISSN: 2347-470X

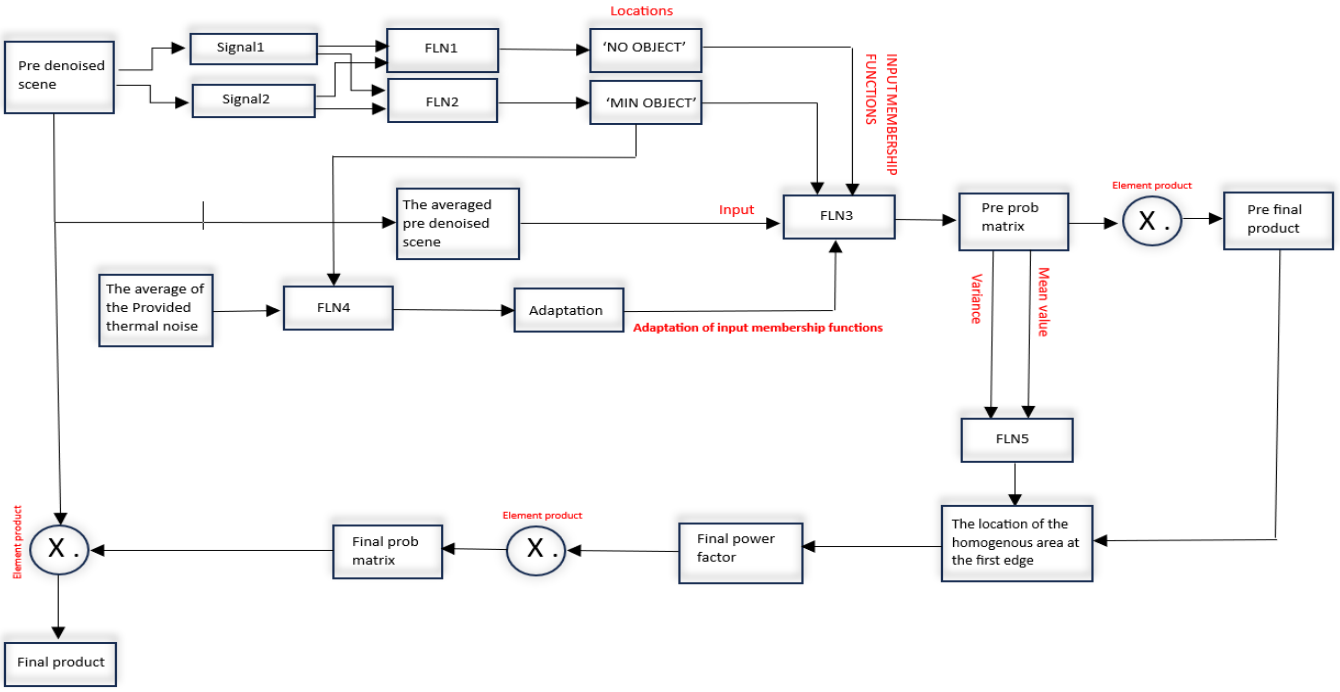

Figure 4. The configuration of the proposed method

$$AK = \frac{1}{9}\sum_{k=1}^{9} RA_k \quad (6)$$

$$\text{ROW AVERAGE(RA)} = \frac{1}{20}\sum_{c=1}^{20} x_{RC}\,, R = 1,2,\ldots \text{row size of the SAR} \quad (7)$$

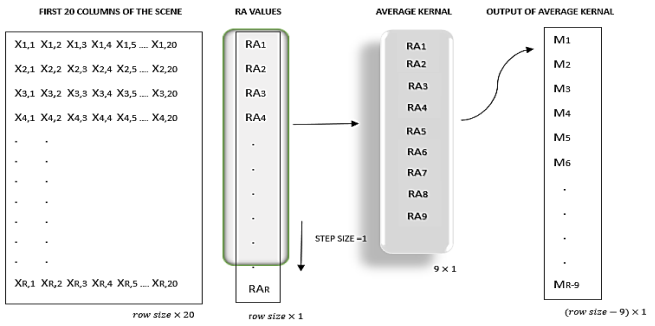

Figure 5. The process of finding the maximum and the minimum TA

Training features from both minimum (minTA) and maximum (maxTA) areas are used to build FLN1's membership functions. These features are extracted using a 9×9 sliding window. The AK method employs a 9×1 sliding window to identifyAK , then MR was calculated using *equation (8)*. minTA and maxTA regions of size 9×20. Therefore, the extraction window must maintain a row size of 9.

$$MR = \frac{1}{9}\sum_{n=1}^{n} MAX\ \&\ MIN[\,[\frac{1}{9}\sum_{m=1}^{m} x_{m_n}]]n = 1,..,9. \quad (8)$$

The feature was chosen to be the MEAN (mean), which is a traditional average filter, the average filter can reduce the speckle noise, therefore, it was chosen to build FLC1. The features from the minTA and maxTA are shown in *figure 6 (a,b)*.

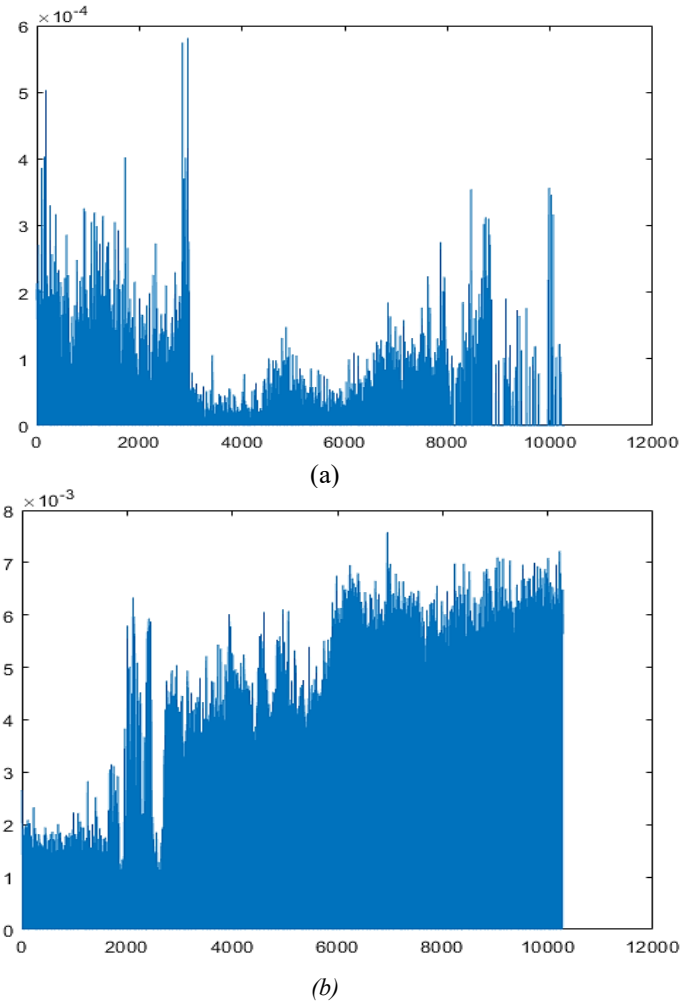

(a)

(b)

Figure 6. The feature from the minTA, and maxTA

FOREX Publication
Open Access | Rapid and quality publishing
International Journal of Electrical and Electronics Research (IJEER)
Research Article | Volume 14, Issue 1| Pages 38-55|e-ISSN: 2347-470X

The EF will have 11 values for each 20 columns, due to the size of the used sliding window, the remaining 9 values are zeros. Each minTA maxTA periods of (20 columns) has maximum and minimum points.

The extracted features from maxTA, where each period includes both maximum and minimum values. The variation and the mean of each period are used to construct two fuzzy logic networks: FLN1 and FLN2. Signal1 represents the period-wise variation, while Signal2 is obtained by subtracting mean values of maxTA from the corresponding local maxima in minTA. These two signals, shown in *figures 7*, form the input membership functions for FLN1 and FLN2.

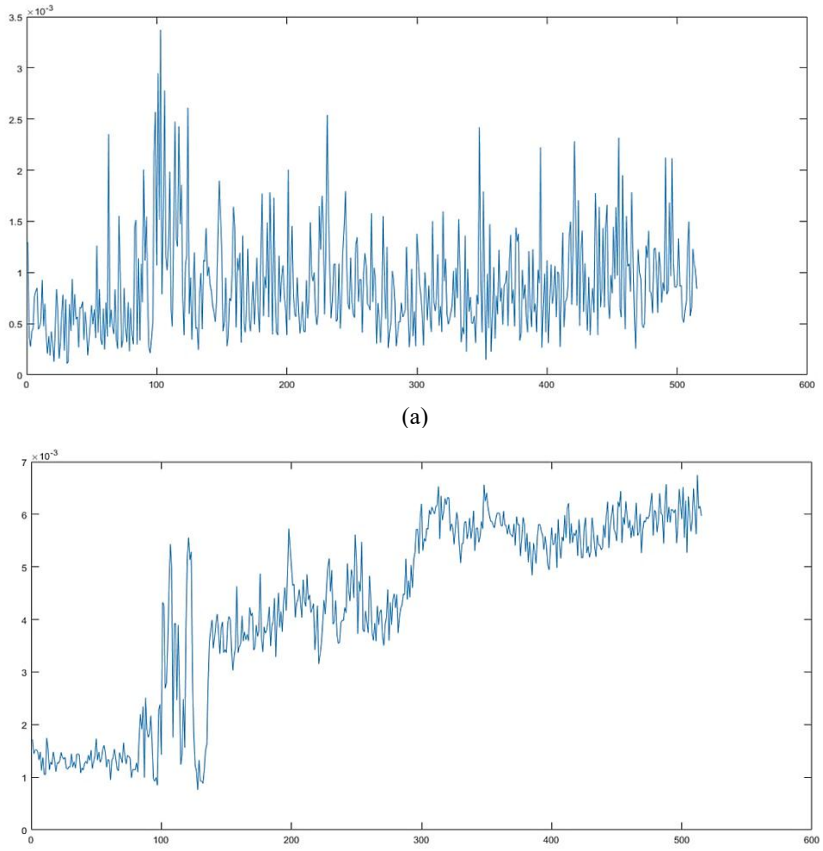

(a)

(b)

Figure 7(a). The variation from the maxTAEF (signal1), and *(b)* The mean values of each period of the maxTAEF subtracted from the maximum values of the minTAEF (signal2)

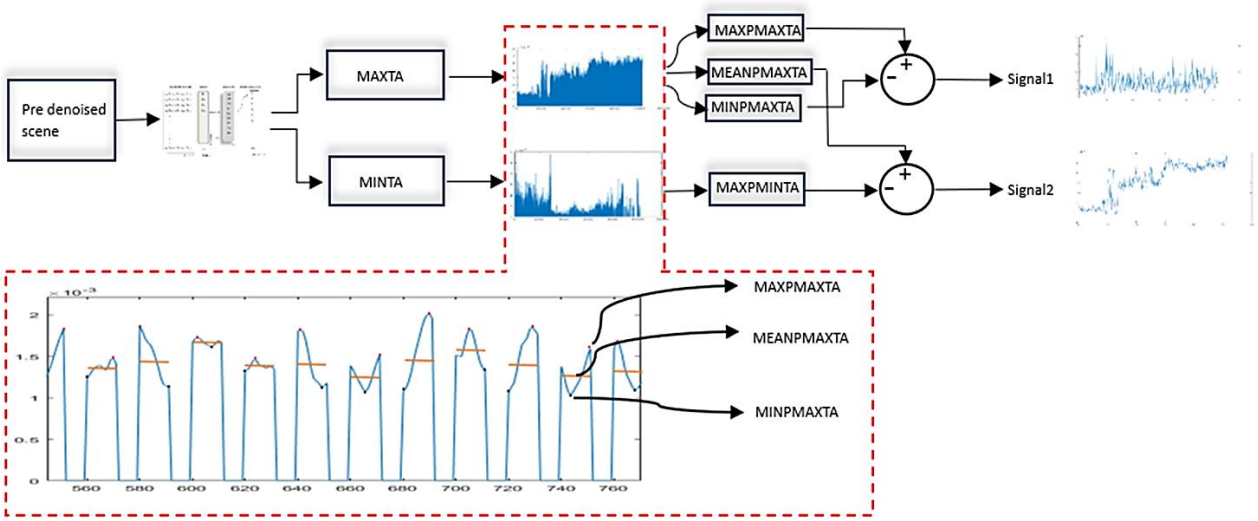

Figure 8. The method is used to obtain Signal1 and Signal2 from the maxTA and minTA

FOREX Publication
Open Access | Rapid and quality publishing
International Journal of Electrical and Electronics Research (IJEER)
Research Article | Volume 14, Issue 1| Pages 38-55|e-ISSN: 2347-470X

Both FLN1 and FLN2 are MIMO SUGENO fuzzy logic controllers. FLN1 was built to find factor2, and FLN2 was built to find factor3. *Figure 9*, shows how the input membership functions for FLN1 are constructed based on these two signals. Factor2 is the mean value of signal1, and factor3 is the maximum value of signal1. The second input of FLN1 was built as the first input but by using signal2. The LOW, MID, and HIGH membership functions were selected as piecewise-linear (triangular with shoulder sets) because they are computationally light, interpretable, and sufficiently flexible for monotonic thresholding; their breakpoints are anchored to the data-driven factors (minimum/mean/maximum), which makes the controller self-scaled for different scenes and sub-swaths without requiring manual tuning.

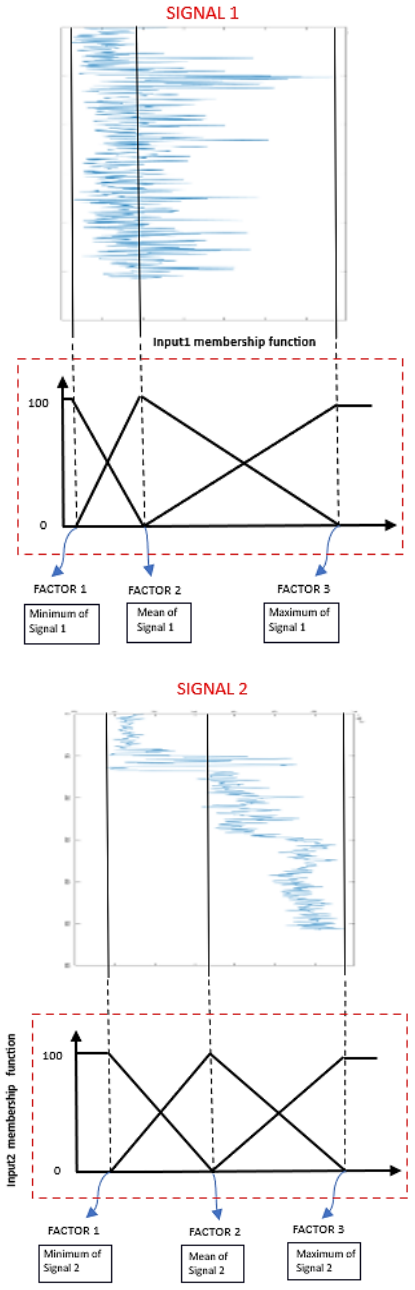

Figure 9. input's membership functions of FLN1 and FLN2

The rules were built to be suitable for many cases. So, for the 'no object' location the mean should be LOW, and the variation also should also be LOW, but for the 'min object' location the mean should be LOW, and the variation should be HIGH. These rules follow the logical characteristics of HV backscatter, open water and noise-only areas shows a weak and relatively stable responses, while the minimum detectable ice introduces local fluctuations even when the mean intensity remains low. Therefore, in FLN1 the rule surface assigns MAX only when both Signal1 and Signal2 are LOW, and gradually reduces the output to MEAN/REMAIN as one of the inputs increases to avoid selecting textured ice as shown in *table 1*. In FLN2 the score is maximized for the (LOW, HIGH) combination to emphasize the minimum detectable object as shown in *table 2*. By applying these logical rules, the method would be able to cover many SAR image cases while keeping the inference monotonic and free of contradictory decisions. Sugeno inference system used REMAIN is zero, MEAN is 0.5 and MAX is 1. The rules of FLN1 and FLN2 are shown in *table 1*, and *table 2* respectively.

Table 1. The rules of FLN1 'no object'

Rule	Signal1	Signal2	Then
1	Low	Low	Max
2	Low	Mid	Mean
3	Low	High	Remain
4	Mid	Low	Mean
5	Mid	Mid	Mean
6	Mid	High	Remain
7	High	Low	Remain
8	High	Mid	Remain
9	High	High	Remain

Table 2. The rules of FLN2 'min object'

Rule	Signal1x	Signal2	Then
1	Low	Low	Remain
2	Low	Mid	Mean
3	Low	High	Max
4	Mid	Low	Remain
5	Mid	Mid	Mean
6	Mid	High	Mean
7	High	Low	Remain
8	High	Mid	Remain
9	High	High	Remain

Inputs from the two training areas:
S1=max(TAmax)-min(TAmax). Within area variation in the maximum training area.
S2=mean(TAmax)-max(TAmin). Saperation between the "max' and the 'min' training area".

FOREX Publication
Open Access | Rapid and quality publishing
International Journal of Electrical and Electronics Research (IJEER)
Research Article | Volume 14, Issue 1| Pages 38-55|e-ISSN: 2347-470X

Where TAmax is the 'maximum training area', and Tamin is the "minimum training area"
Physical meaning of the inputs for "no object".

In a noise-only / no-object situation, the scene is statistically homogeneous, meaning, S_1must be LOW, because there is no structured target inside TA_{max} and thus no meaningful spread beyond speckle/noise. And S_2 must be LOW, because TA_{max} and TA_{min} basically represent the same class (open-water/background), hence there is no separation between them.

Design constraints
Rule-base justification for FLN1
The FLN1 is intentionally designed in a way so the output is a non-increasing function of both inputs, meaning, if either S_1increases (more texture/structure), or S_2increases (stronger separation between "max" and "min" areas), the confidence of the "no object" must not increase. This directly yields the 3×3 rule surface:

Rule (LOW, LOW) → MAX (1): this is the only condition that simultaneously indicates *(i)* homogeneity in $TA_{max}$and *(ii)* no separability between TA_{max} and TA_{min}. thus, it is the strongest evidence of "no object". Any MID in either input → MEAN (0.5): MID indicates mild variability or mild separation that can still happen due to speckle, or small radiometric differences across EW sub-swaths. In these cases, FLN1 will reduce the confidence instead of fully reject the candidate.

Any HIGH in either input → REMAIN (0): HIGH S_1implies textured/structured scattering (ice, ridges, or mixed pixels), and HIGH S_2implies the two areas are separable (i.e., an "object class" exists). In either case, selecting this location as a "no-object" would bias the baseline and introduce error in the adaptive thresholding. Therefore, confidence is forced to zero (REMAIN). So, FLN1's rule table is not arbitrary: it is the minimal monotonic mapping that *(i)* gives a unique strong acceptance for the only consistent no-object signature (LOW, LOW), *(ii)* gives cautious acceptance for borderline cases, and *(iii)* rejects all configurations that contradict the no-object hypothesis.

Rule-base justification for FLN2 (Minimum-detectable-object location)
Similar to FLN1, the design of FLN2 inputs is built with logical roles to assign confidence that the candidate location corresponds to the minimum detectable object (the weakest baby-ice values that is still distinguishable from open water/background). This location is used as the reference "minimum object" response for adaptive tuning.
Physical meaning of the inputs for "minimum detectable object"

The minimum detectable object is characterized by:
(i) Low internal variability (weak, smooth, barely detectable signature), so S_1should be LOW (or at most MID), because the object is not strongly textured or heterogeneous. *(ii)* High separability from the background/open-water training area: S_2should be HIGH, because even the weakest detectable object must still produce a measurable shift of TA_{max}relative to TA_{min}.

Design constraints (again: controlled monotonic behavior)
FLN2 is designed to satisfy two monotonic constraints:
Decreasing with S_1: as variation grows, the candidate is less likely to be "minimum detectable" (it becomes a stronger/complex object or mixed-ice texture).
Increasing with S_2: as separation grows, the candidate is more likely to be an object rather than background.

This explains the key rules:
(LOW, HIGH) → MAX (1): this is the defining signature of a minimum detectable object: the object is weak and smooth (LOW S_1), yet distinguishable from background (HIGH S_2). This is why it is the only MAX rule.

(LOW, MID) and (MID, HIGH) → MEAN (0.5): these are near-boundary cases, (LOW, MID) is slight separability but still weak, could be extremely thin ice, or background affected by calibration/noise so confidence is moderate. (MID, HIGH) is strong separability but moderate internal variation, object exists, but may be slightly stronger than the minimum detectable; still acceptable but not maximal.

All HIGH S_1→ REMAIN (0): a high spread inside TA_{max}indicates heterogeneous scattering (ridging, thicker ice, mixed classes), which contradicts the "minimum detectable" hypothesis. Therefore, FLN2 rejects these cases regardless of S_2.

(LOW, LOW) and (MID, LOW) → REMAIN (0): when $S_2$is LOW, the max and min training areas are not separable; hence no object evidence exists, so the minimum-detectable-object confidence must be zero. So FLN2's rules are the simplest rule surface that peaks only at the physically consistent corner (LOW variation, HIGH separation) and monotonically decreases when the signature moves away from that condition.
The {REMAIN=0, MEAN=0.5, MAX=1} are outputs that used as confidence levels rather than hard classes:
MAX (1): strong evidence that the location satisfies the intended hypothesis (no-object for FLN1; minimum-object for FLN2).
MEAN (0.5): borderline evidence; keeps the candidate in consideration while preventing it from dominating when a stronger match exists.
REMAIN (0): contradictory evidence; the hypothesis should not be used at that location because it risks biasing the downstream adaptive thresholding. This "confidence" interpretation is consistent with the objective of selecting robust reference points rather than performing final segmentation at this stage.

The peak values of FLN1 and FLN2 occur at positions 32 and 63, respectively. Since the pre-denoised scene was averaged initially, these positions correspond to columns 640 and 1260 in the original range direction (32×20 and 63×20). Thus, the 'no object' region spans columns 620–640, and the 'min object' region spans 1240–1260. *Figures 10 (a, b)* show the column elements for these regions.

International Journal of
Electrical and Electronics Research (IJEER)
Research Article | Volume 14, Issue 1| Pages 38-55|e-ISSN: 2347-470X
Open Access | Rapid and quality publishing

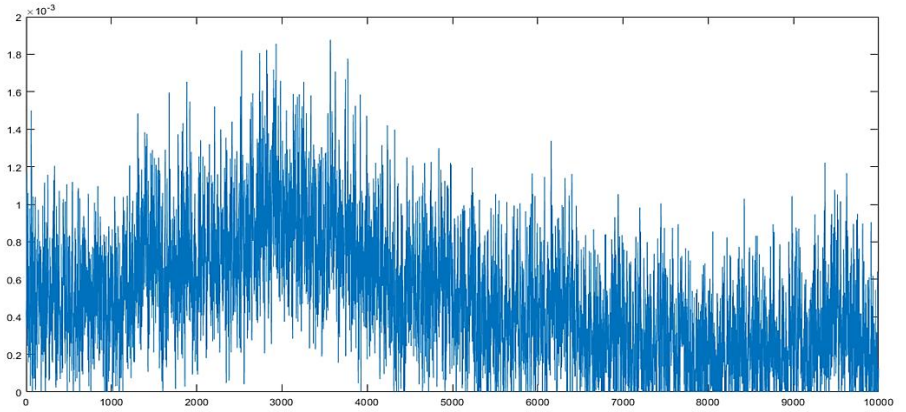

(a)

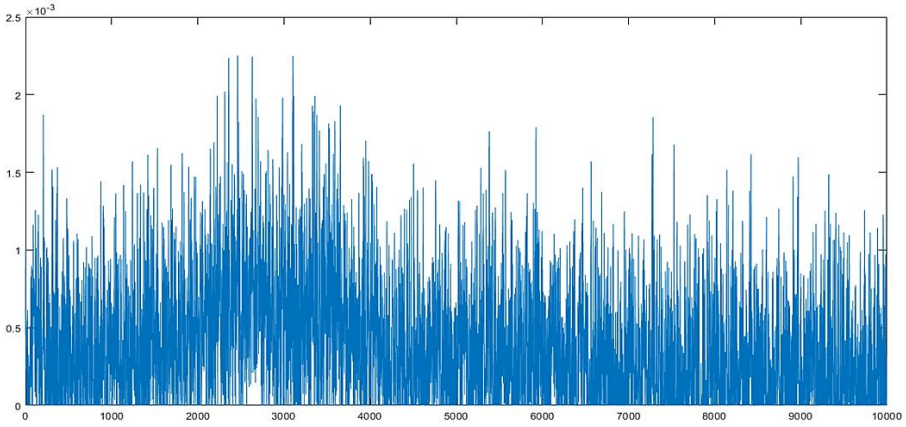

(b)

Figure 10 (a). is the entire columns elements are at "no object" location (FLC2FAC2 vector), and (b) is the entire columns elements at "min object" location (FLC2FAC3 vector)

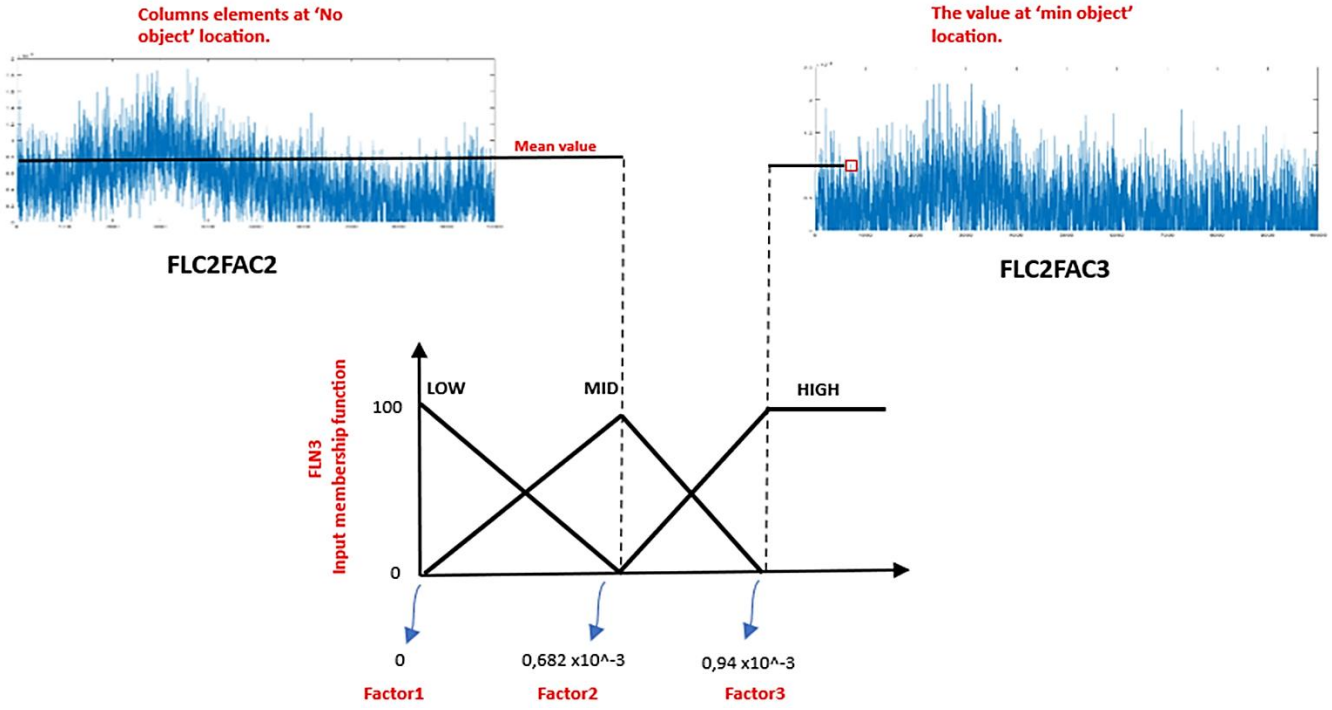

Figure 11. FLN3 input membership functions

FOREX Publication
Open Access | Rapid and quality publishing
International Journal of Electrical and Electronics Research (IJEER)
Research Article | Volume 14, Issue 1| Pages 38-55|e-ISSN: 2347-470X

Based on the roles and the logic discussed above, the design of the "no object" location correspond to an open-water or noise dominant reference block, the second breakpoint of the FLN3 (Factor2) is taken from the signal2 value at the FLN2 selected location for "no object"(FLC2FAC2 vector), and the third breakpoint (Factor3) is taken from the Signal2 value at the FLN selected location for "minimum detectable object" (FLC2FAC3 vector), as shown in Figure 11. In some scenes with fully ice-covered or homogeneous think-ice, a 20x20 open water/noise reference may be absent and the FLN1 may not provide a valid "no object" location, to address this cases and remove this scene dependance, we introduce a fallback mechanism, where the FLN1 peaks confidence is insufficient (or the selected candidate does not satisfy the LOW-LOW homogeneity condition), the FLN1 is not used and instead the Factor2 is derived from the FLN2 reference as Factor2= 0.5.Signal2(at minimum detectable location), while Factor3 remains Signal2 (at minimum detectable location). This choice is conservative because the minimum detectable object response provides an upper bound on the noise-only level, so setting Factor2 at half of this value places the mid breakpoint between Factor1=0 and Factor3, thus preserving the ordering (0 < Factor2 < Factor3), and prevents over-suppression of weak baby-ice signatures while still allowing stable thresholding.

FLN3 is a single input, single output (SISO) fuzzy logic controller (FLC), where the input membership functions are designed similarly to those of FLN1. The inference system used in FLN2 is also Sugeno-based, and the output values of FLN2 are represented as [2, 1, 0], corresponding to thick ice, thin ice, and open water, respectively. The output matrix varies between these values, segmenting the image into three distinct regions. The rules for FLN3 are defined in Table 3. Similarly, FLN3 is a SISO Sugeno inference system, where the inputs consist of three factors: Factor1, the minimum of the averaged ESA-provided thermal noise; Factor2, the thermal noise value at the "min object" location (calculated by FLN1); and Factor3, the maximum of the ESA-provided thermal noise. These inputs are processed to output values that determine the classification of ice regions, specifically targeting thin ice, thick ice, and open water. The rules governing FLN4 are the same as the rules of FLN3.

Table 3. The rules of FLN3 and FLN4

Rule	If Input	Then
1	Low	Remain
2	Mid	Mean
3	High	Max

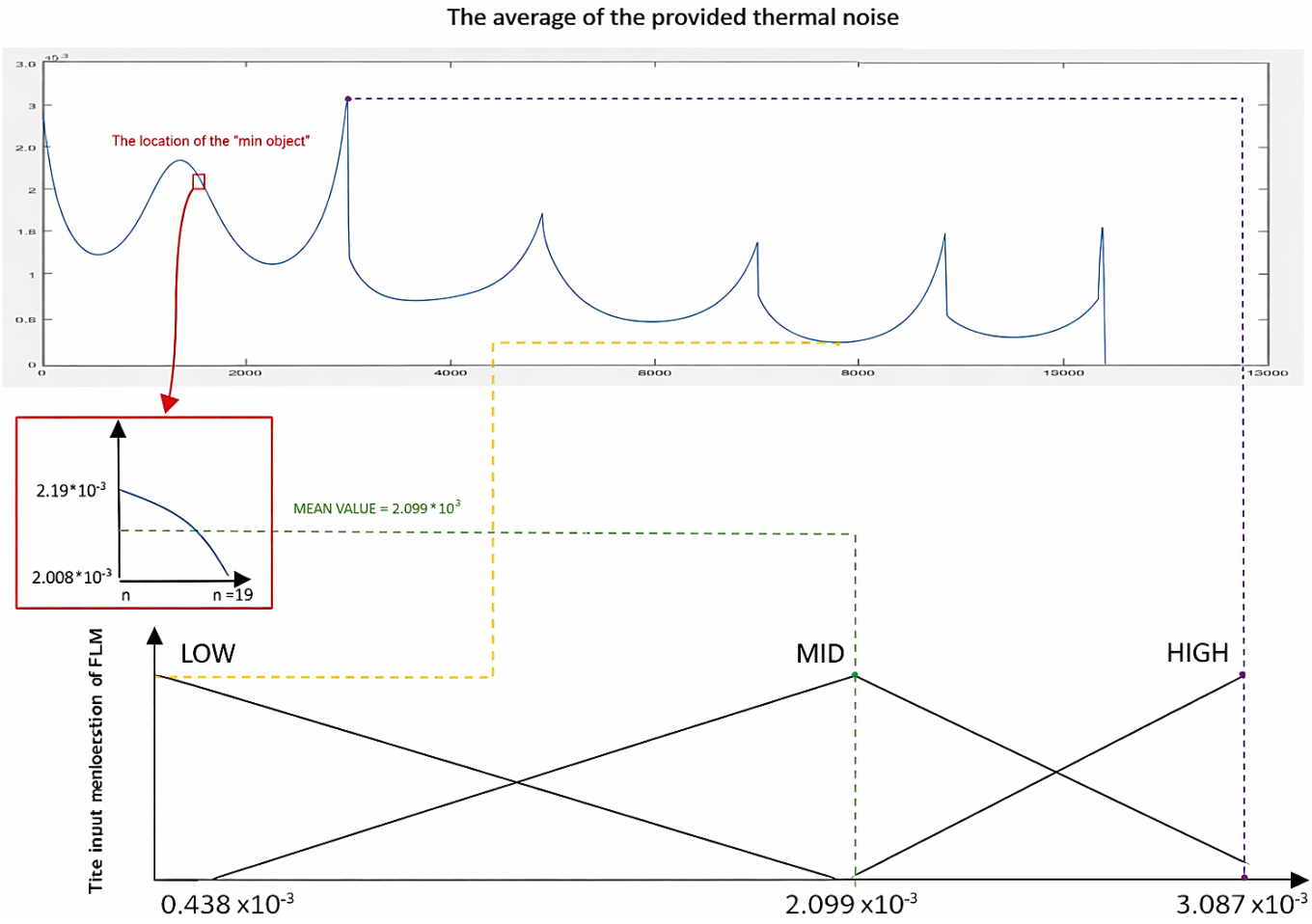

Figure 12. FLN4's input membership functions

FOREX Publication
Open Access | Rapid and quality publishing
International Journal of Electrical and Electronics Research (IJEER)
Research Article | Volume 14, Issue 1| Pages 38-55|e-ISSN: 2347-470X

The FLN4 Is used to give adaptation for FLN3's input membership functions. This is done by expanding the FLN3 breakpoints (Factor2 and Factor3) according to the estimated residual thermal noise level after the pre-denoising. Specifically, FLN4 outputs an adaptation coefficient $\propto$ in the range [0.7, 1.3] (*i.e.*, ±30% around 1), and FLN3's membership function breakpoints are updated as Factor2= $\propto$.Factor2. and Factor3= $\propto$.Factor3, while Factor1 remains fixed at 0. Hence, $\propto > 1$ expands the membership functions to compensate for the under-denoising (higher residual noise), whereas $\propto < 1$ contracts them to avoid over-denoising. The output of the FLN4 is shown in *figure 13*, and the changing in the FLN3's input membership functions are shown in *figure 15*. The ±30% range was selected to provide sufficient flexibility to handle sup-swath-to-sup-swath variations in the ESA-provided thermal-noise vector and incidence-angle-dependent calibration, while preserving the ordering of the breakpoints (Factor1 < Factor2′ < Factor3′) and avoiding unstable rule firing. A narrow range (±10% - 20%), may be insufficient for challenging EW scenes where the residual noise floor differs noticeably across the range direction, whereas a wilder range tends to over-adapt and can either suppress weak baby-ice signature or leaves residual noise. A range of adaptation values were tested to observe their effect on the thin ice regions, as shown in *figure 14*.

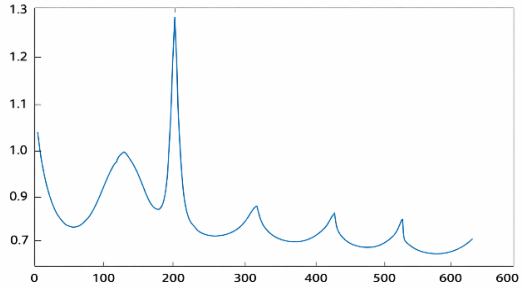

Figure 13. The adaptation from FLN4 (-30% ~ +30%)

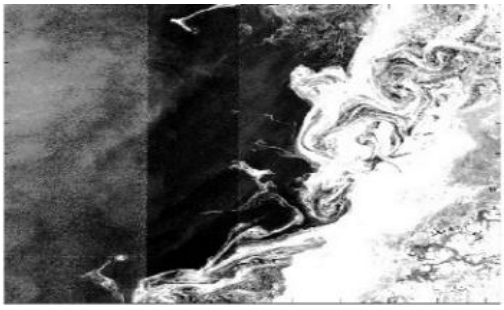

(a)

(b)

(c)

(d)

Figure 14. (a) FLN3 without adaptation factor for the input, (b) with adaptation 1.3 to 0.7, (c) with adaptation 1.3 to 0.5, and (d) with adaptation 1.3 to 0.3

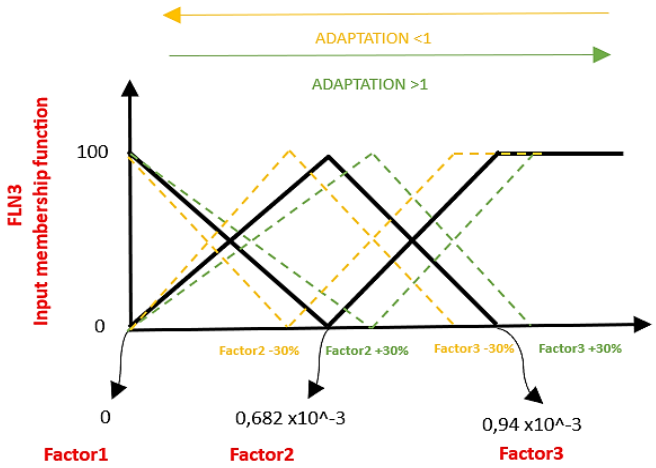

Figure 15. The adaptation from FLN4 on FLN3's membership functions

Since FLN3 was designed to normalize the thermal noise at the "min object" location to a value of 1, the maximum thermal noise value reaches 1.3, and the minimum thermal noise value reaches 0.7

To implement our method, challenging scenes, which include open water, thin ice, and thick ice regions, as shown in *figure 16*. *Figure 17* shows the pre-denoised scene after subtracting the ESA noise vectors using the same method as before. FLN3 was then employed to adapt the input membership functions of FLN2. In these scenes.

FOREX Publication
Open Access | Rapid and quality publishing
International Journal of Electrical and Electronics Research (IJEER)
Research Article | Volume 14, Issue 1| Pages 38-55|e-ISSN: 2347-470X

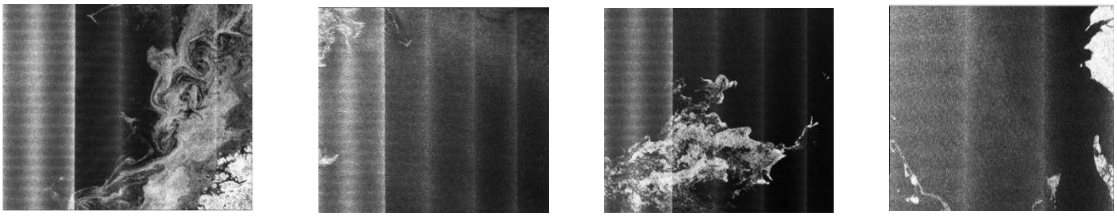

Figure 16. The noisy scenes

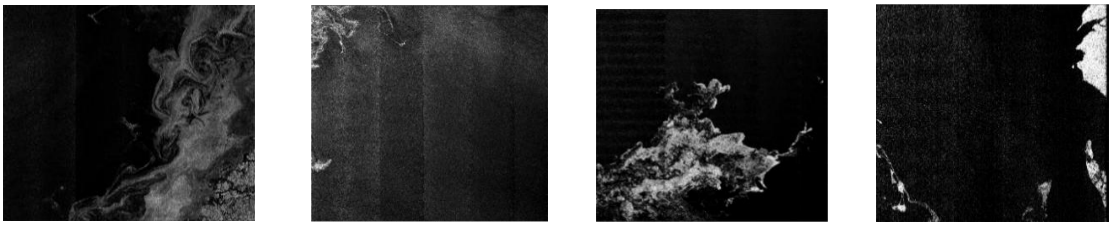

Figure 17. The pre denoised scene after subtracting the ESA noise vectors

The next step is power factor calculation; however, this calculation will be based on the thin ice regions, so FLN5 will be employed. FLN5 is used to identify homogeneous areas between the subswaths, which will then be used for power factor correction. First, homogeneous areas should have a value of 1 (indicating thin ice regions) and exhibit minimal variation. Features will be extracted from the edges of the subswaths. The average pre-denoised scene (divided into 20 segments in the azimuth and range directions) is used for feature extraction, with 3 points before the edge (60 columns in real size) and 7 points after the edge for each boundary. The homogeneous area will be based solely on the probability (prob) matrix and compared with the pre-denoised scene to calculate the power factor. FLN5 is a MISO (multiple-input, single-output) system, although a SISO (single-input, single-output) version of FLN5 can be used, making decisions based only on the variation value. The input membership functions for FLN5 were designed similarly to those of previous FLNs, as shown in *figure 18*.

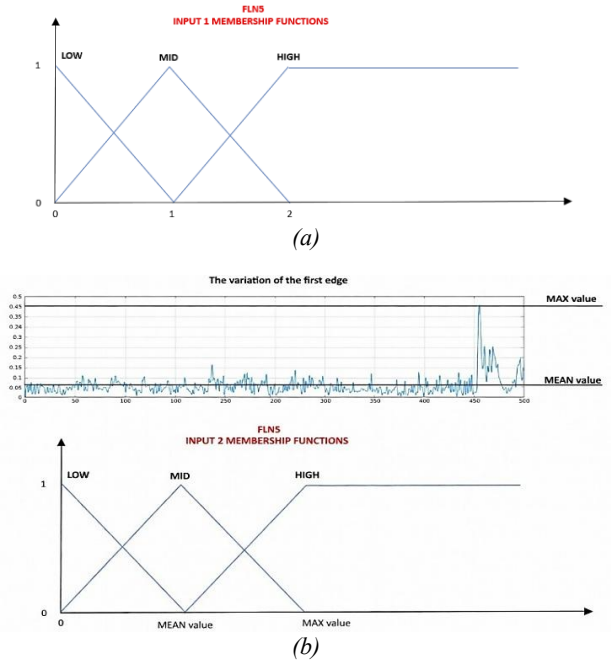

Figure 18. The input membership functions of FLN5

The second input is constructed based on the variation between the first two subswaths. The variation in the probability matrix between these subswaths is shown in *figure 19*. FLN5 is then used to identify homogeneous areas, which have a mean value of 1 and minimal variation, as well as to detect all boundaries between the subswaths. FLN5's rules are shown in *table 4*.

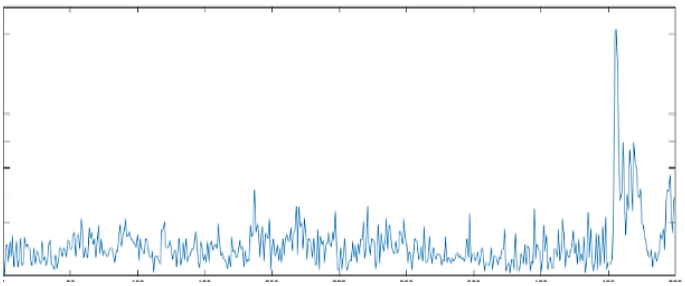

Figure 19. The variance at the first boundary (between 1st and 2nd subswaths)

Table 4. The Rules of FLN5

Rule	Signal1	Signal2	Then
1	Low	Low	Mean
2	Low	Mid	Remain
3	Low	High	Remain
4	Mid	Low	Max
5	Mid	Mid	Mean
6	Mid	High	Remain
7	High	Low	Remain
8	High	Mid	Remain
9	High	High	Remain

The variance and mean were calculated starting 3 points before the edge and 7 points after the edge on the average pre-denoised scene. Each point represents 20 pixels in the original-size scene. The maximum points for each of these vectors represent the locations (referred to as "homolocs") that will be used for the power factor calculation. For Scene 1, the homolocs were found to be [199, 19, 23, 434]. At these "homolocs," the average of the first three points (which are located before the edge) and the

FOREX Publication
Open Access | Rapid and quality publishing
International Journal of Electrical and Electronics Research (IJEER)
Research Article | Volume 14, Issue 1| Pages 38-55|e-ISSN: 2347-470X

average of the remaining seven points (located after the edge) will be calculated. Both the output from FLC2 and the average pre-denoised scene will be used in this calculation, as described in *equation (9)* and *(10)*.

$$power1 = \frac{1}{3}\sum_{1}^{3}\rho_i\,, i = 1,2,3 \quad (9)$$

$$power2 = \frac{1}{7}\sum_{3}^{10}\rho_i\,, i = 3,4,..10 \quad (10)$$

Where ρ_i is the pixel of FLN3 output matrix at the homolocs locations, $power1$ is the average of the 3 pixels before the edges, and $power2$ is the average of the 7 pixels after the edges. The power1 and power2 will be calculated for both the FLN3's output (prob mat), and the averaged pre denoised as it was mentioned. The 3 points before and 7 points after the first edge from the 'probmat' are shown in *figure 20*. The expected values of the thin ice as FLC4 were designed to be around 1, otherwise correction factor should be calculated.

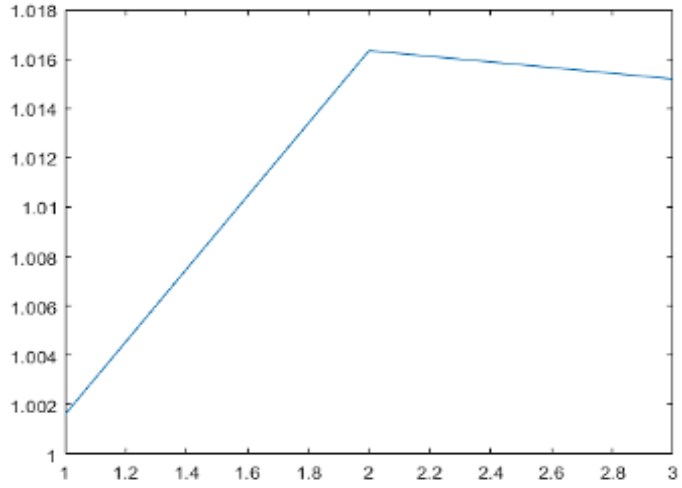

(a)

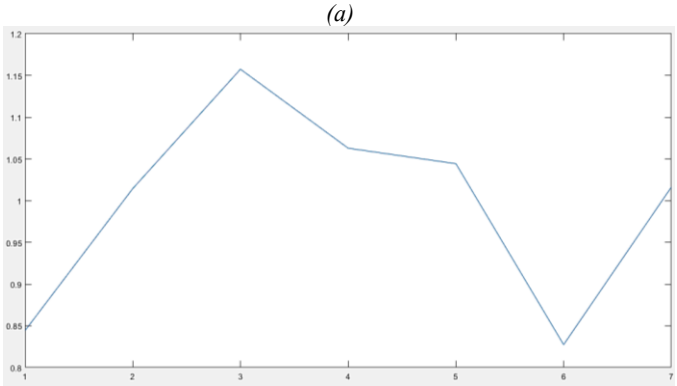

(b)

Figure 20. (a) and (b) the 3 pixels values before and after the 1st edge from the 'probmat' at the 'homoloc', respectively

Power1=[1.0110 0.3067 1.0649 1.3678].

As it is clear that the second sub swath is lower than the others, therefore, the power2 factor must be calculated to ensure that it needs to be leveled up, so thin ice regions could be detectable.

Power2 was calculated to be as follows:

[0.9952 0.4400 0.9435 1.4196]. The final power factor to enhance the thin ice regions was calculated as in *equation (11)*.

$$Final\ power\ factor(i) = \left(\frac{1}{powerfactor1_i} + \frac{1}{powerfactor2i}\right)^{1}/_{2} \quad (11)$$

Where (i) is the subswath. The final power factor was calculated for scene1 [0.9970 2.7666 0.9995 0.7178 1.0000], each value represents the power factor for a subswath in order. The pre prob matrix was calculated by using FLN3 output to be multiplied by the pre denoised scene [see *figure (21)*].

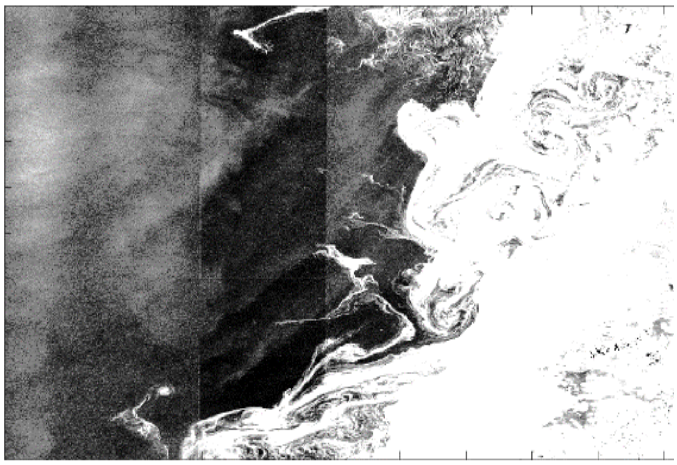

Figure 21. the pre prob matrix (normal prob matrix)

By multiplying the pre prob matrix with the final power factor matrix, the result in *figure (22)* can be obtained.

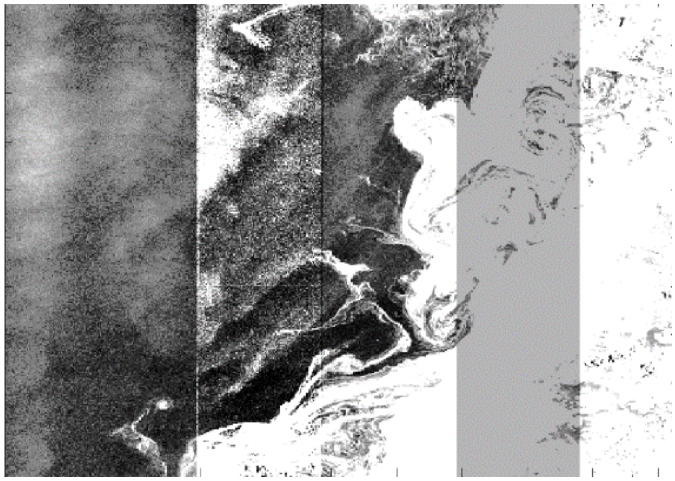

Figure 22. The pre prob matrix after multiplied by final power matrix (final prob matrix)

To compare the result to analyze the effectiveness of using the final power matrix, which was shown in *figure (22)*, normal prob matrix and final prob matrix were multiplied by the pre-denoised scene [See *figures (23)-(24)*].

FOREX Publication
Open Access | Rapid and quality publishing
International Journal of Electrical and Electronics Research (IJEER)
Research Article | Volume 14, Issue 1| Pages 38-55|e-ISSN: 2347-470X

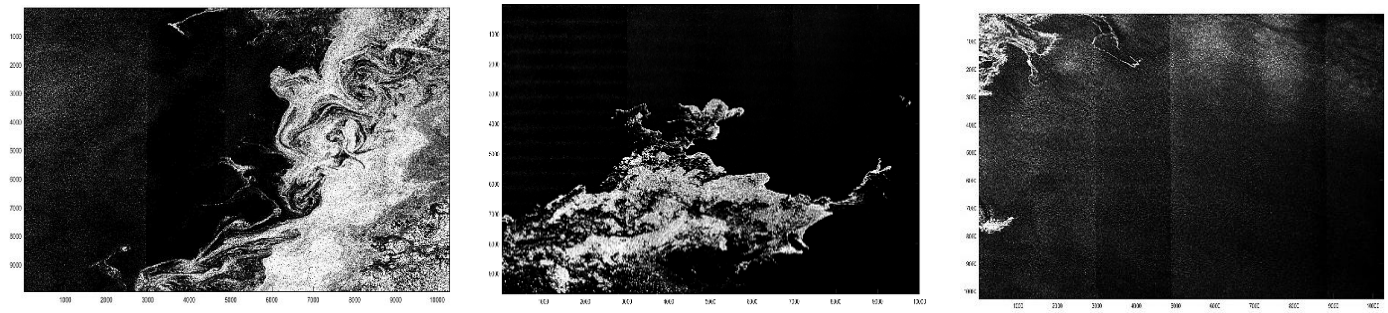

Figure 23. The final product of the proposed method

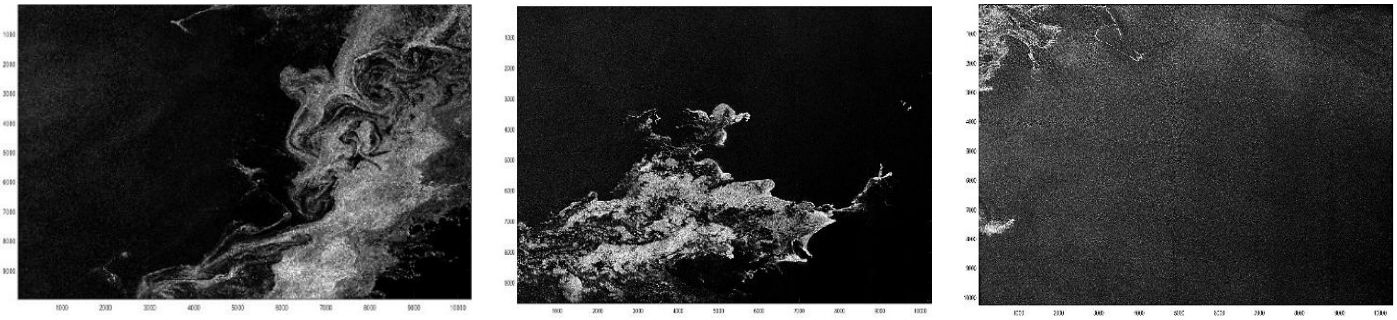

Figure 24. The final products by using the method which was presented in [5]

To make the method independent of Signal1, and thereby applicable to various sea ice scenarios, an additional step is required, as illustrated in *figure 25*.

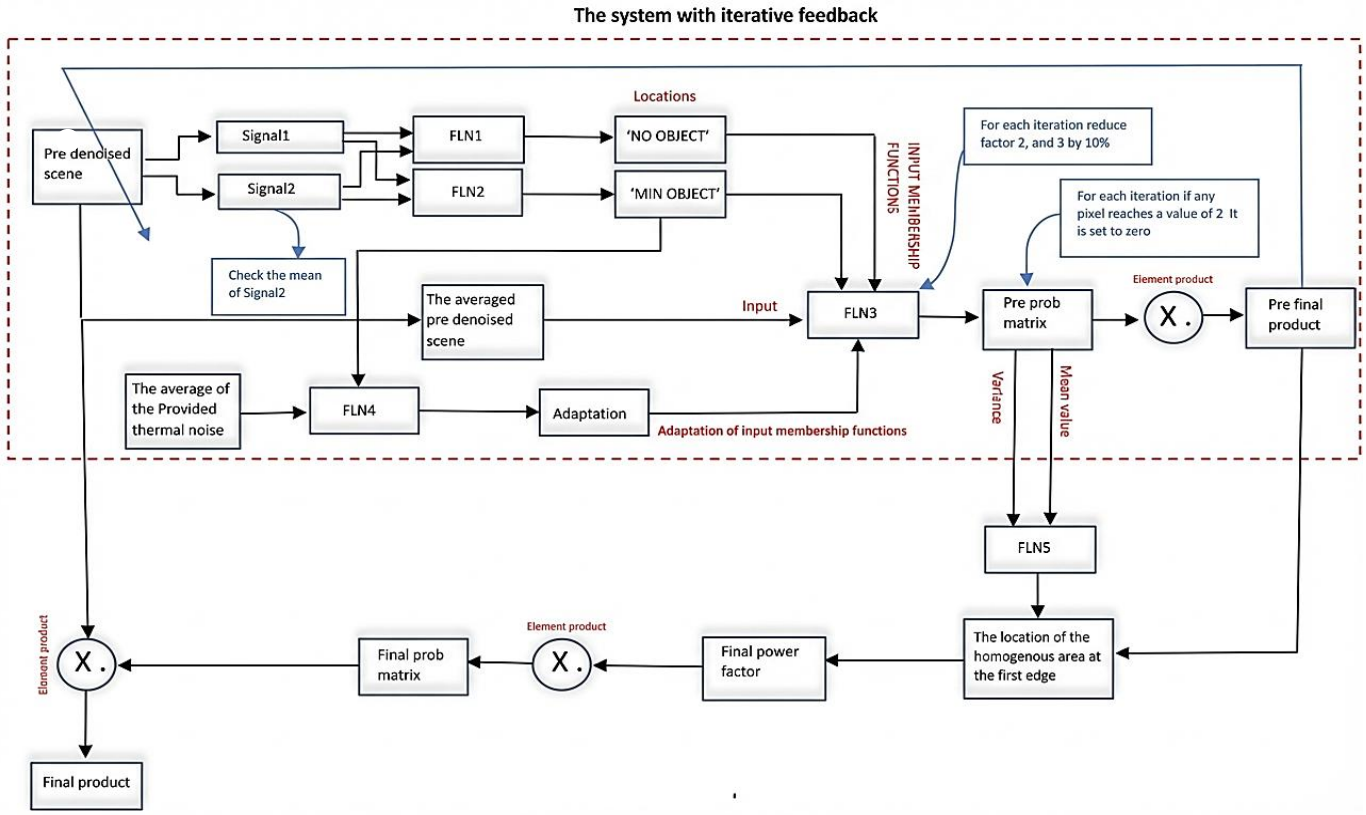

Figure 25. The iterative system, where the pre final product is replaced with the pre denoised scene

FOREX Publication
Open Access | Rapid and quality publishing
International Journal of Electrical and Electronics Research (IJEER)
Research Article | Volume 14, Issue 1| Pages 38-55|e-ISSN: 2347-470X

The primary objective of the feedback mechanism is to make the system independent of Signal1, which was initially used to build FLN1, and to stabilize the refinement across different EW scenes and sub-swaths. This is achieved by progressively reducing the mean level of Signal2 computed on the maximum training area (maxTA), bringing it closer to a physically meaningful reference derived from the minimum detectable object identified by FLN2.

Let *Wi* denote the block (or window) location of the minimum detectable object (from FLN2). and let the reference be as described in *equation (12)*.

$$r_2 = \text{Signal2(Wi)} \tag{12}$$

At iteration t, the mean of Signal2 over the maximum training area is

$$\mu_2^{(t)} = \frac{1}{|\text{number of (maxTA)}|}\sum_{x\in\text{maxTA}} \text{Signal2}^{(t)}(x) \tag{13}$$

Driving $\mu_2^{(t)}$toward r_2 has the following interpretation: when the mean of Signal2 converges toward the "minimum detectable object" level, it indicates that the scene has been sufficiently suppressed such that only open water and the weakest ice responses remain, and further refinement yields diminishing changes.

Error function

To formalize this behavior, we define the mean-alignment error:

$$e^{(t)} = \mu_2^{(t)} - r_2 \quad , \quad E^{(t)} = \frac{|e^{(t)}|}{|r_2|+\varepsilon}, \tag{14}$$

where ε is a small constant (e.g., 10^{-6}) to avoid division by zero. $E^{(t)}$ is a normalized, scene-robust scalar that directly measures how close the current maxTA Signal2 level is to the reference level.

Stopping criterion (convergence)

The iterative refinement is terminated using a clear convergence/stability criterion rather than a fixed iteration count:

$$E^{(t)} \le \tau_E \text{ OR } |E^{(t)} - E^{(t-1)}| \le \tau_\Delta \text{ for } L \text{ consecutive iterations,}$$

with an additional maximum iteration number of $K_{\max}$. The first condition stops when the mean is sufficiently close to the reference, while the second stops when improvements become negligible (plateau behavior). This makes the number of iterations a data-dependent and automatically determined by convergence.

Convergence behavior and stability (discussion)

The feedback update replaces the next iteration input with the current refined output using a mask-based suppression step:

$$I^{(t+1)} = I^{(t)} \odot M^{(t)}, 0 \le M^{(t)} \le 2, \tag{15}$$

where $I^{(t)}$is the pre-denoised scene at iteration t, $M^{(t)}$is the FLN3-derived feedback mask after mapping the thick-ice class to zero, and $\odot$ denotes element-wise multiplication. Because $M^{(t)} \in [0,2]$.In addition, the implementation uses a decreasing gain $w^{(t)}$(damping) to reduce update aggressiveness over iterations, which mitigates oscillations and promotes stable convergence. Consequently, $E^{(t)}$decreases rapidly in the early iterations and then saturates, and further iterations provide negligible change, this behavior is explicitly captured by the stopping rule.

Algorithm: Iterative feedback refinement

1. Run the first pass to obtain maxTAand the minimum detectable object block location Wi (FLN2).
2. Set $r_2 = \text{Signal2(Wi)}$,
3. For $t = 1$to: $E^{(t)} \le \tau_E$ OR $|E^{(t)} - E^{(t-1)}| \le \tau_\Delta$
   - Recompute Signal2$^{(t)}$from current $I^{(t)}$.
   - Compute $\mu_2^{(t)}$, $E^{(t)} = \frac{|\mu_2^{(t)} - r_2|}{|r_2|+\varepsilon}$.
   - If $E^{(t)} \le \tau_E$: stop.
   - If $|E^{(t)} - E^{(t-1)}| \le \tau_\Delta$: stableCount++ else stableCount=0.
   - If stableCount $\ge L$: stop.
   - Apply FLN3 (with the iteration's MF scaling) → mask $M^{(t)}$.
   - Map thick-ice label to 0 for feedback, update $I^{(t+1)} = I^{(t)} \odot M^{(t)}$.
4. Output final product $I^{(t)}$.

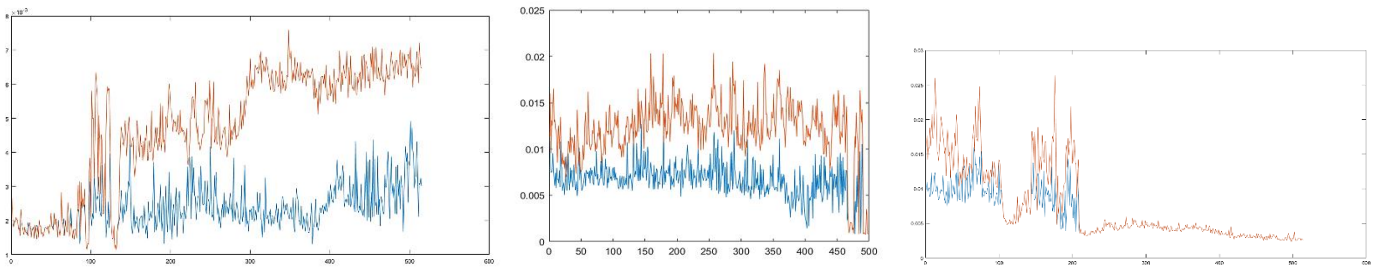

Figure 26. Red line represents Signal2 which was shown in *figure 7(b)* before the iterations, and the blue line represents the same feature after the iterations

FOREX Publication
Open Access | Rapid and quality publishing
International Journal of Electrical and Electronics Research (IJEER)
Research Article | Volume 14, Issue 1| Pages 38-55|e-ISSN: 2347-470X

As shown in *figure 16*, the noisy scenes do not provide any clear information about thin ice regions, even after subtracting the noise matrices provided in the notated files the thin ice regions remain undetectable as it is clearly shown in *figure 16*. In this research, the proposed iterative system was applied to obtain the pre-final product, revealing the baby ice regions, as indicated in *figure 27*.

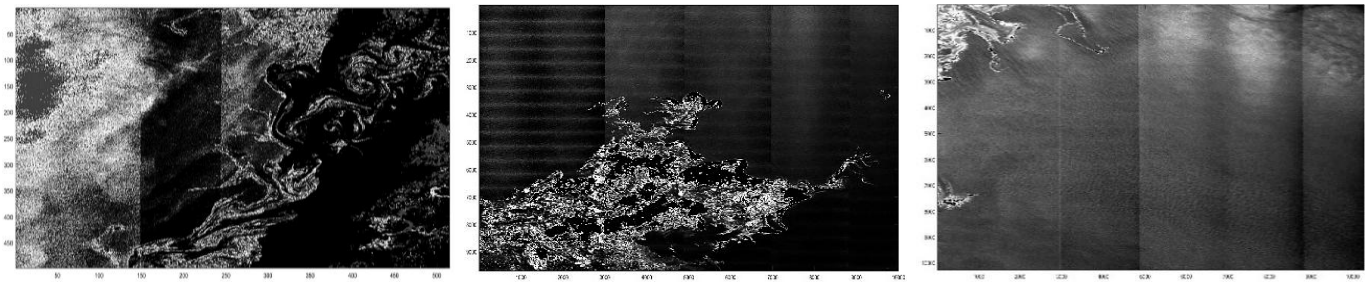

Figure 27. The final product using the iterative system

At the end of each iteration, values reaching 2 are set to zero, forming a zero matrix. These zero matrices are then multiplied together to generate *figure 28*, representing the thick ice regions (black areas).

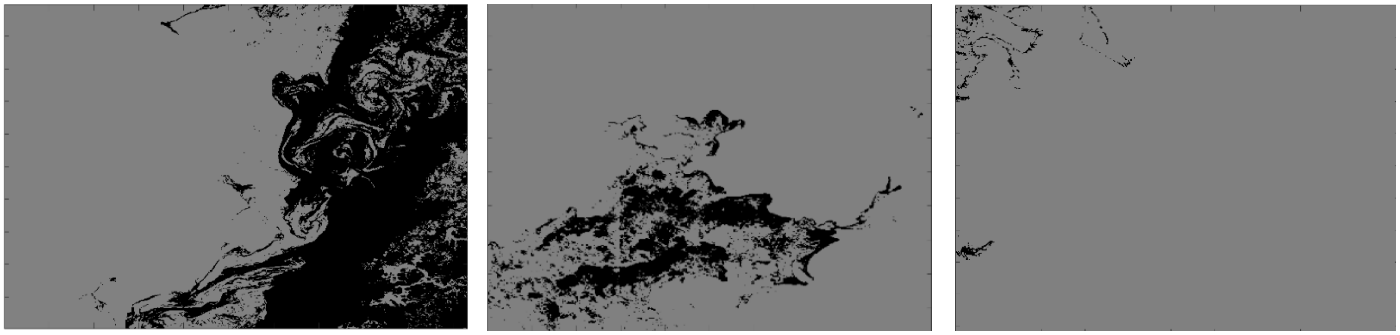

Figure 28. The values that reached zero after the iterations, representing thick ice

4. EXPERIMENTS

The experimental section evaluates the proposed multi-stage adaptive fuzzy-network framework on Sentinel-1 EW HV sea-ice scenes containing open water, baby-ice, and thicker ice regions. the entire experiments follow a consistent processing pipeline and parameter setting across scenes, including the same block/window size, the FLN1–FLN5 rule bases, and the iterative feedback refinement with the defined stopping criterion. Performance is reported using quantitative noise-suppression and stability measures computed on homogeneous regions of interest, together with qualitative visual comparisons that focus on preserving ice–water boundaries and enhancing the visibility of weak baby-ice signatures.

The Test Data that were used in this research are provided in *table 5*.

Table 5. Test Data

Scene ID	Sensor	Beam Mode	Acquisition_DateTime
Scene 1	Sentinel 1A	EW	20180902T165032
Scene 2	Sentinel 1A	EW	20220323T211643
Scene 3	Sentinel 1A	EW	20220402T101947

4.1. Quantitative Metrics

Because ENL and speckle statistics are meaningful only in homogeneous regions, we computed quantitative metrics on carefully selected regions of interest (ROIs). For each scene, we selected K ROIs (rectangular patches) representing homogeneous areas like open water, ROI coordinates were defined on the original HV image and reused unchanged for all methods (original, baselines, proposed). This ensures that any improvement is attributable to denoising rather than ROI selection bias. *Figure 6* illustrates ROI locations on the full scene and corresponding zoom-in patches before and after processing.

Figure 6 Full-scene HV image with ROI locations (rectangles), and zoom-in patches for the same ROIs before and after denoising.

We report three objective metrics that do not require external ground truth. Let Idenote the linear intensity values within an ROI, with mean μ, standard deviation σ, and variance σ^2.

5. RESULTS

Tables (6)-(8) report MEAN, STD, and SNR for multiple scenes, and *figures (29)-(31)* show the selected ROIs and the SNR location for each scene. The proposed method consistently improves homogeneity in HV imagery, reflected by increased SNR, reduced MEAN, and STD relative to both the ESA provided noise vectors data and method represented in [5].

FOREX Publication
Open Access | Rapid and quality publishing
International Journal of Electrical and Electronics Research (IJEER)
Research Article | Volume 14, Issue 1| Pages 38-55|e-ISSN: 2347-470X

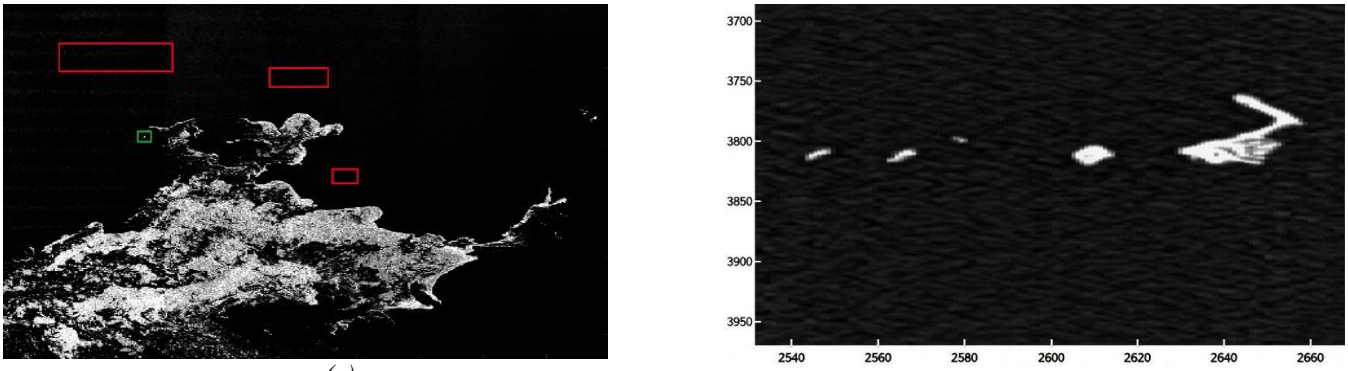

(a) (b)

Figure 29. (a) The red boxes are the used ROIs locations for Mean and STD calculations, and green box is the ROI location used for SNR calculation. (b) Is the zoomed in SNR patch

Table 6. Scene1 Metrics calculated for the most homogeneous open-water area and SNR

Method	Size		Mean	Std	SNR
Method [5]	Rows=4700~5200	Columns =5400~6100	3.9827e-04	1.2624e-16	0.0112862
	Rows=2000~2500	Columns=4200~5100	5.8540e-04	2.5803e-15	
	Rows=1500~2050	Columns=1200~3000	0.0010	1.2325e-14	
ESA (annotated files)	Rows=4700~5200	Columns =5400~6100	3.6169e-04	1.8900e-16	0.0211939
	Rows=2000~2500	Columns=4200~5100	6.3712e-04	1.7934e-16	
	Rows=1500~2050	Columns=1200~3000	0.00139	1.9325e-14	
DnCNN	Rows=4700~5200	Columns =5400~6100	3.9871e-04	1.2438e-16	0.0210911
	Rows=2000~2500	Columns=4200~5100	5.8613e-04	2.4498e-15	
	Rows=1500~2050	Columns=1200~3000	1.7310e-04	1.1393e-14	
Our Method	Rows=4700~5200	Columns =5400~6100	**6.3752e-05**	**5.1962e-19**	**0.0228437**
	Rows=2000~2500	Columns=4200~5100	**1.3610e-04**	**4.0646e-17**	
	Rows=1500~2050	Columns=1200~3000	**1.6526e-04**	**4.7806e-16**	

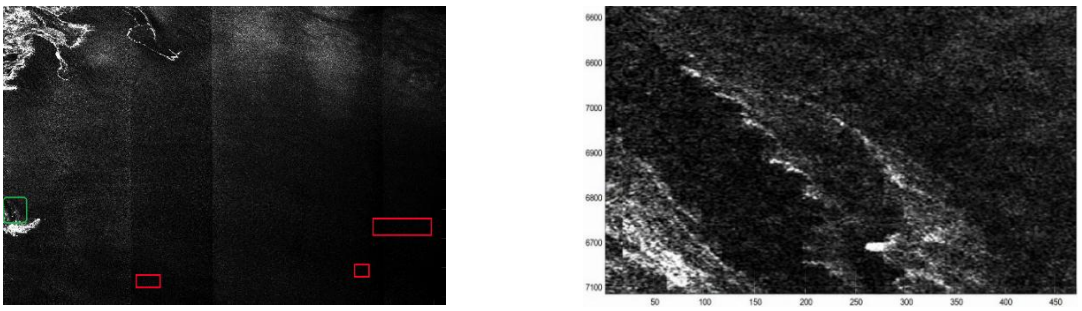

(a) (b)

Figure 30. (a) The red boxes are the used ROIs locations for Mean and STD calculations, and green box is the ROI location used for SNR calculation. (b) Is the zoomed in SNR patch

Table 7. Scene2 Metrics calculated for the most homogeneous open-water area and SNR

Method	Size		Mean	Std	SNR
Method [5]	Rows=9000~9500	Columns=8800~9500	5.5383e-04	3.0102e-15	0.0100138
	Rows=9200~9700	Columns=3200~4100	0.0017	5.2831e-15	
	Rows=7500~8050	Columns=8900~10200	6.1928e-04	1.1037e-15	
ESA (annotated files)	Rows=9000~9500	Columns=8800~9500	6.8283e-04	4.2624e-15	0.0147107
	Rows=9200~9700	Columns=3200~4100	0.00189	4.2660e-14	
	Rows=7500~8050	Columns=8900~10200	3.5753e-04	1.1037e-15	
DnCNN	Rows=9000~9500	Columns=8800~9500	0.0013	8.2666e-15	0.00116849
	Rows=9200~9700	Columns=3200~4100	0.0023	5.1925e-15	
	Rows=7500~8050	Columns=8900~10200	0.0013	1.0573e-15	
Our Method	Rows=9000~9500	Columns=8800~9500	**1.5908e-04**	**3.6755e-17**	**0.0177165**
	Rows=9200~9700	Columns=3200~4100	**4.7921e-04**	**3.9792e-16**	
	Rows=7500~8050	Columns=8900~10200	**1.9497e-04**	**9.4114e-17**	

FOREX Publication
Open Access | Rapid and quality publishing
International Journal of Electrical and Electronics Research (IJEER)
Research Article | Volume 14, Issue 1| Pages 38-55|e-ISSN: 2347-470X

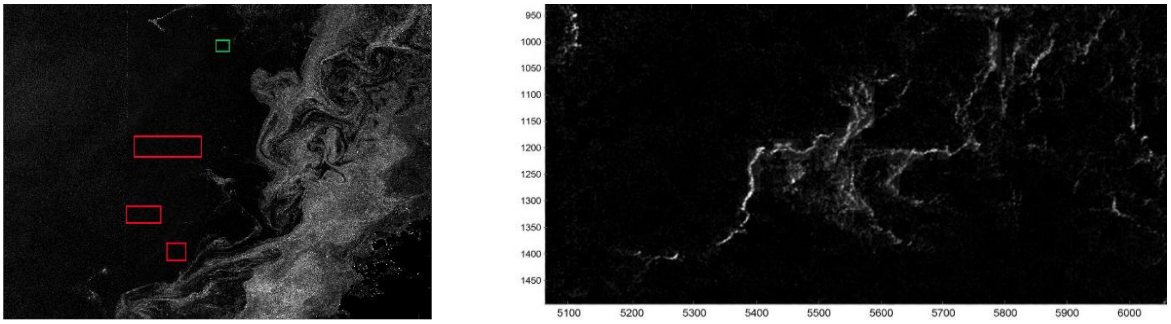

(a) (b)

Figure 31. (a) The red boxes are the used ROIs locations for Mean and STD calculations, and green box is the ROI location used for SNR calculation. (b) Is the zoomed in SNR patch

Table 8. Scene3 Metrics calculated for the most homogeneous open-water area and SNR

Method	Size		Mean	Std	SNR
Method [5]	Rows=7700~8200	Columns=3600~4300	2.8370e-04	1.9269e-16	0.00578349
	Rows=6800~7300	Columns=3100~4000	3.4935e-04	8.6728e-17	
	Rows=4500~5050	Columns=3300~4500	3.6182e-04	7.0033e-17	
ESA (annotated files)	Rows=7700~8200	Columns=3600~4300	9.1619e-05	7.6811e-17	0.00675223
	Rows=6800~7300	Columns=3100~4000	1.1084e-04	1.2214e-16	
	Rows=4500~5050	Columns=3300~4500	1.2694e-04	1.2756e-16	
DnCNN	Rows=7700~8200	Columns=3600~4300	8.8417e-05	7.2669e-17	0.00615609
	Rows=6800~7300	Columns=3100~4000	1.1069e-04	1.1664e-16	
	Rows=4500~5050	Columns=3300~4500	1.2852e-04	1.2198e-16	
Our Method	Rows=7700~8200	Columns=3600~4300	**1.7568e-05**	**1.3311e-17**	**0.0107652**
	Rows=6800~7300	Columns=3100~4000	**3.1456e-05**	**3.3669e-17**	
	Rows=4500~5050	Columns=3300~4500	**4.1128e-05**	**1.1205e-17**	

6. DISCUSSION

In this paper, a new adaptive thresholding and thin ice detection method for sea ice SAR images was developed using a self-built fuzzy logic controller network. The proposed method effectively reduces thermal noise and the scalloping effect in HV-polarized extra-wide (EW) SAR images, particularly when identifying the locations of "thick ice," "thin ice," and "open water." To evaluate its performance, several experiments were conducted using Sentinel-1 SAR images, focusing on noise reduction, feature extraction, and overall denoising effectiveness. The method's performance was assessed by comparing the denoised images with the ESA provided denoised images. The results demonstrated a significant improvement in image quality, with a notable reduction in noise levels. This improvement facilitated better identification of sea ice regions, including previously unobservable "baby ice" areas, which are essential for accurate sea ice monitoring.

7. CONCLUSIONS

This study presented an adaptive denoising and thresholding framework to mitigate thermal noise and the scalloping effect in HV-polarized Sentinel-1 EW sea-ice SAR imagery. By leveraging a multi-stage fuzzy logic controller network, the approach estimates scene-specific noise behavior through data-driven selection of “no object” and “minimum object” locations and applies a correction factor to refine noise suppression without external tuning. Across multiple scenes, ROI-based open-water statistics (mean and standard deviation) and an SNR measure demonstrate improved homogeneity relative to the ESA/SNAP noise-vector correction workflow and the recent EW sea-ice method in [5], while also providing competitive behavior when compared with the DnCNN baseline under the same ROI protocol. Visual inspection further confirms that weak baby-ice structures become more discernible without blurring ice–water boundaries. The method is designed for sea-ice scenes where open water, thin ice, and thick ice may coexist; when a clear open-water reference is absent, a conservative fallback based on the minimum detectable object is used to construct the required reference for the subsequent stage, enabling operation in heavily ice-covered scenes, although performance may degrade in fully homogeneous thick-ice conditions. Finally, while DnCNN offers a representative CNN-denoising reference, building and evaluating a fully supervised deep-learning model specifically for EW HV sea-ice remains challenging due to the scarcity of paired clean targets and large-scale, reliable thin-ice annotations. Future work will focus on establishing representative benchmarks and exploring self-/weakly-supervised strategies tailored to EW sea-ice noise characteristics.

Conflicts of Interest: Authors stated that no conflict of Interest.

REFERENCES

[1] N. Ivanova, O. M. Johannessen, L. T. Pedersen and R. T. Tonboe, "Retrieval of Arctic Sea Ice Parameters by Satellite Passive Microwave Sensors: A Comparison of Eleven Sea Ice Concentration Algorithms," in IEEE Transactions on Geoscience and Remote Sensing, vol. 52, no. 11, pp. 7233-7246, Nov. 2014, doi: 10.1109/TGRS.2014.2310136.

[2] L. Hermozo, L. Eymard and F. Karbou, "Modeling Sea Ice Surface Emissivity at Microwave Frequencies: Impact of the Surface Assumptions

and Potential Use for Sea Ice Extent and Type Classification," in IEEE Transactions on Geoscience and Remote Sensing, vol. 55, no. 2, pp. 943-961, Feb. 2017, doi: 10.1109/TGRS.2016.2616920.

[3] C. Li, S. Park, D. -J. Kim and J. Kim, "A Deep Learning Based Self-Evolving Oil Spill Detection Algorithm Using Sentinel-1 SAR Images," IGARSS 2023 - 2023 IEEE International Geoscience and Remote Sensing Symposium, Pasadena, CA, USA, 2023, pp. 1289-1292, doi: 10.1109/IGARSS52108.2023.10281695.

[4] J. Liu, L. Liu and J. Xiao, "Ellipse Polar Encoding for Oriented SAR Ship Detection," in IEEE Journal of Selected Topics in Applied Earth Observations and Remote Sensing, vol. 17, pp. 3502-3515, 2024, doi: 10.1109/JSTARS.2024.3352098.

[5] Y. Sun and X. M. Li, "Denoising Sentinel-1 Extra Wide Mode Cross-Polarization Image Over Sea Ice," IEEE Trans. Geosci. Remote Sens., vol. 59, no. 3, pp. 2116-2130, 2021.

[6] Y. Gao, C. Guan, J. Sun, and L. Xie, "A wind speed retrieval model for sentinel-1A EW mode cross-polarization images," Remote Sens., vol. 11, no. 2, p. 153, Jan. 2019.

[7] L. Liu, Z. Jia, J. Yang and N. K. Kasabov, "SAR Image Change Detection Based on Mathematical Morphology and the K-Means Clustering Algorithm," in IEEE Access, vol. 7, pp. 43970-43978, 2019, doi: 10.1109/ACCESS.2019.2908282.

[8] J. Karvonen, "Baltic Sea ice concentration estimation using Sentinel-1 SAR and AMSR2 microwave radiometer data," IEEE Trans. Geosci. Remote Sens., vol. 55, no. 5, pp. 2871–2883, May 2017.

[9] M. Iqbal, J. Chen, W. Yang, P. Wang, and B. Sun, "Kalman filter for removal of scalloping and inter-scan banding in scansar images," Prog.Electromagn. Res., vol. 132, pp. 443–461, 2012.

[10] R. Romeiser, J. Horstmann, M. J. Caruso, and H. C. Graber, "A descalloping postprocessor for ScanSAR images of ocean scenes," IEEE Trans.Geosci. Remote Sens., vol. 51, no. 6, pp. 3259–3272, Jun. 2013.

[11] J. -W. Park, A. A. Korosov, M. Babiker, S. Sandven and J. -S. Won, "Efficient Thermal Noise Removal for Sentinel-1 TOPSAR Cross-Polarization Channel," in IEEE Transactions on Geoscience and Remote Sensing, vol. 56, no. 3, pp. 1555-1565, March 2018, doi: 10.1109/TGRS.2017.2765248.

[12] J.-W. Park, A. A. Korosov, M. Babiker, S. Sandven, and J.-S. Won,"Efficient thermal noise removal for Sentinel-1 TOPSAR crosspolarization channel," IEEE Trans. Geosci. Remote Sens., vol. 56, no. 3, pp. 1555–1565, Mar. 2018.

[13] J.-W. Park, J.-S. Won, A. A. Korosov, M. Babiker, and N. Miranda, "Textural noise correction for Sentinel-1 TOPSAR cross-polarization channel images," IEEE Trans. Geosci. Remote Sens., vol. 57, no. 6, pp. 4040–4049, Jun. 2019.

[14] J. Li, L. Lin, M. He, J. He, Q. Yuan and H. Shen, "Sentinel-1 Dual-Polarization SAR Images Despeckling Network Based on Unsupervised Learning," in IEEE Transactions on Geoscience and Remote Sensing, vol. 62, pp. 1-15, 2024, Art no. 5106315, doi: 10.1109/TGRS.2024.3404405.

[15] I. -C. Sang and W. R. Norris, "An Adaptive Image Thresholding Algorithm Using Fuzzy Logic for Autonomous Underwater Vehicle Navigation," in IEEE Journal of Selected Topics in Signal Processing, vol. 18, no. 3, pp. 358-367, April 2024, doi: 10.1109/JSTSP.2024.3426484.

[16] X. Yan, "Application of Image Segmenting Technology Based on Fuzzy C-Means Algorithm in Competition Video Referee," in IEEE Access, vol. 12, pp. 34378-34389, 2024, doi: 10.1109/ACCESS.2024.3355465.

[17] L. Reznik, Fuzzy Controllers Handbook: How to Design Them, How They Work. Elsevier, 1997.

[18] A. K. Pandey, H. R. S. S. N. Chatla, M. Pandya, A. Farhan M A and A. S. Rana, "Image Edge Detection Using Fuzzy Logic Controller," 2023 International Conference on Recent Advances in Electrical, Electronics & Digital Healthcare Technologies (REEDCON), New Delhi, India, 2023, pp. 508-513, doi: 10.1109/REEDCON57544.2023.

[19] S. Singha, T. J. Bellerby and O. Trieschmann, "Satellite Oil Spill Detection Using Artificial Neural Networks," in IEEE Journal of Selected Topics in Applied Earth Observations and Remote Sensing, vol. 6, no. 6, pp. 2355-2363, Dec. 2013, doi: 10.1109/JSTARS.2013.2251864.

[20] M. Chowdhury, Junbin Gao and R. Islam, "Fuzzy logic-based filtering for image de-noising," 2016 IEEE International Conference on Fuzzy Systems (FUZZ-IEEE), Vancouver, BC, Canada, 2016, pp. 2372-2376, doi: 10.1109/FUZZ-IEEE.2016.7737990.

[21] P. Q. Lee, L. Xu and D. A. Clausi, "Estimating Noise Floor in Sentinel-1 Images with Linear Programming and Least Squares," in IEEE Transactions on Geoscience and Remote Sensing, vol. 60, pp. 1-14, 2022, Art no. 5212414, doi: 10.1109/TGRS.2021.3101455.

[22] G. Zhou et al., "HPHR-SAR-Net: Hyperpixel High-Resolution SAR Imaging Network Based on Nonlocal Total Variation," in IEEE Journal of Selected Topics in Applied Earth Observations and Remote Sensing, vol. 16, pp. 8595-8608, 2023, doi: 10.1109/JSTARS.2023.3295728.

[23] R. Shang et al., "SAR Image Segmentation Based on Constrained Smoothing and Hierarchical Label Correction," in IEEE Transactions on Geoscience and Remote Sensing, vol. 60, pp. 1-16, 2022, Art no. 5102216, doi: 10.1109/TGRS.2021.3076446.

[24] F. Gu, H. Zhang and C. Wang, "A Two-Component Deep Learning Network for SAR Image Denoising," in IEEE Access, vol. 8, pp. 17792-17803, 2020, doi: 10.1109/ACCESS.2020.2965173.

[25] S. Liu, S. Tian, Y. Zhao, Q. Hu, B. Li and Y. -D. Zhang, "LG-DBNet: Local and Global Dual-Branch Network for SAR Image Denoising," in IEEE Transactions on Geoscience and Remote Sensing, vol. 62, pp. 1-15, 2024, Art no. 5205515, doi: 10.1109/TGRS.2024.3362510.

[26] P. T. Hien and I. -P. Hong, "Millimeter Wave SAR Imaging Denoising and Classification by Combining Image-to-Image Translation with ResNet," in IEEE Access, vol. 11, pp. 70203-70215, 2023, doi: 10.1109/ACCESS.2023.3293644.

[27] L. Wang, Z. Niu, R. Shang, Y. Qin, L. Wang, and H. Chen, "High-resolution mapping of forest canopy height using machine learning by coupling ICESat-2 LiDAR with Sentinel-1, Sentinel-2, and Landsat-8 data," Int. J. Appl. Earth Obs. Geoinf., vol. 92, p. 102163, 2020. [Online]. Available: https://doi.org/10.1016/j.jag.2020.102163.

[28] E. Alhatami, B. Uzair Aslam, M. Huang and S. Feng, "Advanced Fuzzy Denoising Technique for Agricultural Remote Sensing: Modified Partition Filter for Suppressing Impulsive," in IEEE Access, vol. 12, pp. 159025-159035, 2024, doi: 10.1109/ACCESS.2024.3447704

[29] S. Shi, S. Yan, Y. Wang and Y. Li, "Medical Ultrasound Image Denoising Based on Fuzzy Logic," 2014 Fifth International Conference on Intelligent Systems Design and Engineering Applications, Hunan, China, 2014, pp. 611-614, doi: 10.1109/ISDEA.2014.143.

[30] S. Dhar and M. K. Kundu, "Interval Type-2 Fuzzy Set and Theory of Weak Continuity Constraints for Accurate Multiclass Image Segmentation," in IEEE Transactions on Fuzzy Systems, vol. 28, no. 9, pp. 2151-2163, Sept. 2020, doi: 10.1109/TFUZZ.2019.2930932.

[31] C. Guan, S. Wang and A. W. -C. Liew, "Lip Image Segmentation Based on a Fuzzy Convolutional Neural Network," in IEEE Transactions on Fuzzy Systems, vol. 28, no. 7, pp. 1242-1251, July 2020, doi: 10.1109/TFUZZ.2019.2957708.

[32] U. Javed, M. M. Riaz, A. Ghafoor and T. A. Cheema, "SAR image segmentation based on active contours with fuzzy logic," in IEEE Transactions on Aerospace and Electronic Systems, vol. 52, no. 1, pp. 181-188, February 2016, doi: 10.1109/TAES.2015

[33] Subhedar, M., & Birajdar, G. (2013). Comparison of mamdani and sugeno inference systems for dynamic spectrum allocation in cognitive radio networks. Wireless personal communications, 71, 805-819.

[34] SNAP - ESA Sentinel Application Platform v{9}, http://step.esa.int (access on 14/02/2024).